1 **A Sequential Triple-Drug Strategy for Selective Targeting of p53-Mutant Cancers**

2

3 Mohammed M. Alruwaili[1,2], Yanqi Guo[1], Justin Zonneville[1], Thomas Melendy[3], Robert M.
4 Straubinger[4,5], Barbara A. Foster[5], Priyanka Rajan[1], Henry Withers[6], Sarah Chatley[7], Renuka
5 Iyer[7], Christos Fountzilas[7*], and Andrei V. Bakin[1*]

6 Author affiliation: [1]Department of Cancer Genetics and Genomics, Roswell Park Comprehensive
7 Cancer Center, Buffalo, New York 14263; [2]Department of Medical Laboratory Technology,
8 College of Applied Medical Science, Northern Border University, Arar City, Saudi Arabia;
9 [3]Department of Microbiology and Immunology, University at Buffalo, 14214, [4]Department of
10 Pharmaceutical Sciences, University at Buffalo, 14214; [5]Department of Pharmacology and
11 Therapeutics, [6]Department of Biostatistics and Bioinformatics, [7]Department of Medicine,
12 Roswell Park Comprehensive Cancer Center, Buffalo, New York 14263.

13 [*]**Corresponding authors:** Andrei V. Bakin, Department of Cancer Genetics and Genomics, Tel.
14 (716) 845-1033; e-mail: Andrei.Bakin@Roswellpark.org; and Christos Fountzilas, Department
15 of Medicine, Tel. (716)845-8974, e-mail: Christos.Fountzilas@Roswellpark.org, Roswell Park
16 Comprehensive Cancer Center, Buffalo, New York 14263

17 **The Lead Contact**: Andrei V. Bakin, Department of Cancer Genetics and Genomics, Tel. (716)
18 845-1033; e-mail: Andrei.Bakin@Roswellpark.org

19

20 **Conflict of interest**: The authors declare no conflicts of interest.
21 **Data availability**: The data, analytical methods, and study materials will be made available to
22 other researchers through supplemental material or upon request.

23

SUMMARY

The tumor suppressor *TP53* gene (p53) is mutated in most human malignancies; however, existing treatment options are largely ineffective, lack selectivity, and cause toxic side effects. To address these clinical problems, we developed a sequential triple-drug strategy for p53 mutant cancer cells. Here we show that a combination of a thymidine analogue (TAS102) plus PARP inhibitor (PARPi) promotes formation of DNA double-strand breaks (DSBs) and G2-arrest specifically in p53 mutant cancer cells. Transcriptome analysis revealed that TAS102-PARPi treatment of p53 mutant cells did not repress DNA replication but activated DSB repair and blocked the mitotic program, consistent with G2-arrest. In contrast, TAS102-PARPi treatment of normal p53 wild-type cells resulted in a temporal G1-arrest and rapid recovery of cell cycle capacity after drug withdrawal. In p53 mutant cancer cells, subsequent blocking of a G2-checkpoint kinase, such as WEE1, released these G2-arrested cells into mitosis, leading to massive cell death. Delayed administration of a G2-kinase inhibitor provides time for p53 wild-type cells to repair DNA, thereby minimizing toxicity to normal tissues. This sequential triple-drug strategy exhibited robust efficacy in preclinical models of colorectal and pancreatic cancers and was well tolerated in mice. Together, our findings illustrate a promising triple-drug strategy for targeting p53 mutant malignancies.

KEYWORDS: pancreatic cancer, colorectal cancer, poly (ADP-ribose) polymerase, DNA damage, 5-fluorodeoxyuridine, PARP inhibitor, TAS102, trifluorothymidine

ABBREVIATIONS: BER, base excision repair; CRC, colorectal adenocarcinoma; DSB, double-strand break; EdUrd, 5-ethynyl-2'-deoxyrudine; TFT, trifluorothymidine; HR, homological recombination; MMR, mismatch repair; mPFS, median progression-free survival; OS, overall survival; PDAC, pancreatic ductal adenocarcinoma; SSB, single-strand break.

48 **INTRODUCTION**

49 Colorectal cancer (CRC) and pancreatic ductal adenocarcinoma (PDAC) are among the
50 leading causes of cancer-related mortality worldwide, posing significant global health
51 challenges[1]. Despite improvements in early detection [2], CRC remains a considerable clinical
52 burden, as the majority of patients are diagnosed at advanced stages or progress to metastatic
53 disease after initial treatment[3]. The 5-year overall survival (OS) rate for patients with metastatic
54 disease is less than 15% [4, 5]. PDAC is an aggressive cancer characterized by rapid disease
55 progression, early metastasis, and limited response to conventional therapies[6]. The 5-year OS
56 rate for PDAC for all stages combined remains under 10% despite the use of multi-agent
57 chemotherapy regimens [6, 7]. For patients with chemotherapy-refractory CRC or PDAC, there are
58 currently no FDA-approved therapies that extend overall survival beyond 3 months[5, 7]. These
59 poor clinical outcomes suggest the need for more effective therapeutic strategies that target the
60 molecular vulnerabilities of these cancers.

61 The tumor suppressor *TP53* gene is mutated in most cancers, including CRC and PDAC, and
62 mutant p53 (p53mut) contributes to cancer progression and poor response to therapy[8, 9]. p53
63 protein is critical for maintaining genomic stability by regulating DNA repair and cell cycle
64 control at the G1/S checkpoint in response to DNA damage[10]. Despite ample knowledge of the
65 functional consequences of p53 mutations, therapeutic approaches targeting p53mut cancers
66 have been largely unsuccessful, and p53 status is largely ignored in the clinical management of
67 patients[11]. Cancer cells with mutant p53 show greater reliance on the G2 checkpoint due to the
68 loss of G1-checkpoint control. This vulnerability of p53mut tumors has been explored with
69 agents targeting the G2 checkpoint alone or in combination with chemotherapeutics, such as
70 doxorubicin and carboplatin[12-14]. The major limitations of these approaches are the low

71 selectivity of these therapeutics for p53 status and the high hematologic and organ toxicities in
72 combination therapy[15, 16]. Therapeutic strategies with enhanced selectivity towards p53mut
73 cancers are needed to improve treatments of these malignancies [10].

74 Recently, we developed a two-drug therapeutic strategy that selectively induced DNA
75 damage in p53mut cancer cells [17, 18]. This strategy combines the thymidine analog TAS102,
76 which acts as an inducer of DNA single-strand breaks (SSBs) through post-replicative DNA
77 repair, and PARP inhibitor (PARPi) which acts as an amplifier of DNA damage by converting
78 SSBs to more lethal double-strand DNA breaks (DSBs)[17, 18]. TAS102-PARPi treatment induces
79 G1-arrest in wild-type p53 (p53WT) cells, while p53mut cells exhibit high DSB levels, G2-
80 arrest, and increased cell death [18]. The inducer-amplifier strategy showed greater efficacy in
81 p53mut cancer models, including CRC and PDAC, compared to either drug alone, while no
82 major toxicities were observed in mice [17, 18]. This two-drug strategy is being tested in a first-in-
83 human Phase I clinical trial for patients with refractory CRC using the TAS102-talazoparib
84 combination (NCT04511039)[19]. Preliminary data showed no significant signs of toxicity and
85 improved median progression-free survival (mPFS) compared to historical mPFS for TAS102
86 alone[19].

87 Here, we show that TAS102-PARPi treatment induces prolonged G2-arrest in p53mut cancer
88 cells even after drug washout, while non-tumor p53WT cells rapidly repair their DNA and re-
89 enter the cell cycle. The ATR-WEE1 signaling axis is critical for G2-arrest in response to
90 TAS102-PARPi in p53mut cancer cells. Following TAS102-PARPi treatment, a selective
91 inhibitor of WEE1 kinase released p53mut cells with unrepaired DNA into mitosis, leading to
92 cell death. This sequential approach combining TAS102-PARPi treatment with a WEE1 inhibitor

93 showed greater tumor control in preclinical models than either treatment alone. The sequential
94 triple-drug regimen was well tolerated in animals even after extended administration.
95

96 **MATERIALS AND METHODS**

97 **Cell culture models**

98 The human CRC cell lines HT29 (RRID:CVCL_0320) and DLD1 (RRID:CVCL_0248), human
99 non-tumor breast epithelial MCF10A (RRID: CVCL_0598) and human breast cancer MDA-MB-
100 231 (RRID:CVCL_0062) were obtained from the American Type Culture Collection (ATCC,
101 Manassas, VA, USA) and cultured as recommended by ATCC. The human CRC cell lines
102 HCT116, HCT116-p53(-/-; KO), HCT116-p53(R248W/-), SW48, and SW48-p53(-/-; KO) were
103 obtained from Dr. Bert Vogelstein, Johns Hopkins University. Human CRC RKO and RKO-
104 p53(-/-, KO) cell lines were obtained from Dr. Alessandro Carugo, IRBM European School of
105 Molecular Medicine, Italy. The details of the genetic information for the cell line and patient-
106 derived xenograft (PDX) models are presented in **Key Resources Table**. All human cell lines
107 were authenticated using short tandem repeat profiling by ATCC or the Roswell Park Genomic
108 Shared Resource within the last three years. The cells were routinely screened for mycoplasma,
109 and all studies made use of mycoplasma-free cells. Cell cultures were maintained in media and
110 incubated as recommended by ATCC.

111 **Cell-derived xenografts in mice**

112 Female SCID/CB17 mice (6−8-week-old) were obtained from a colony of SCID/CB17 mice that
113 were bred and maintained at the Animal Facility of the Roswell Park Comprehensive Cancer
114 Center. Animals were kept in microinsulator units and were provided with food and water *ad*
115 *libitum* according to a protocol and guidelines approved by the Institute Animal Care and Use
116 Committee (IACUC). The facility was certified by the American Association for Accreditation

117 of Laboratory Animal Care (AAALAC) and in accordance with the current regulations and
118 standards of the US Department of Agriculture and the US Department of Health and Human
119 Services. Mice were inoculated subcutaneously into the left flank with exponentially growing
120 HT29 tumor cells at (1×10^6/mouse). Tumor growth was monitored by measuring tumor
121 diameters with electronic calipers twice/a week. The volume was calculated using the formula
122 (length) × $(\text{width})^2/2$. The weights of mice were measured twice per week. Once the tumor
123 volume reached 50-100 mm^3, mice were randomly assigned (n = 8-10/group) into four treatment
124 arms: (1) vehicle control, (2) WEE1 inhibitor (WEE1i, adavosertib, MK-1775, 40-60 mg/kg), (3)
125 TAS102-talazoparib (TAS102: 50 mg/kg, talazoparib: 0.150 mg/kg), and (4) sequential regimen
126 (TAS102-talazoparib for one week followed by WEE1i in the second week). TAS102 and
127 talazoparib were dissolved in 12% HPCD (2-hydroxypropyl)-β-cyclodextrin in DPBS, whereas
128 MK-1775 was prepared in 5% DMSO, 40% PEG300, 5% Tween-80, and 50% saline. All drugs
129 were freshly prepared and administered via oral gavage on a 5-days-on, 2-days-off schedule. At a
130 tumor diameter of $2cm^3$, mice were euthanized and subjected to necropsy and organ collection.
131 Tumor growth assessment was stopped once a mouse reached the endpoint (typically in a
132 vehicle-treated cohort) while survival data were still collected in the study. Tumor tissues were
133 collected by snap-freezing in liquid nitrogen for RNA and protein analyses. Blood was collected
134 for CBC by cardiac puncture.

135 **Patient Derived Xenograft (PDX)**

136 Donor and experimental pancreatic patient-derived xenografts (PDAC-PDX-14312-4p) were
137 implanted subcutaneously into SCID mice, whereas colorectal patient-derived xenografts (CRC
138 PDX-3B1-29-RP-3p; APC E1353*, KRAS-G12D, TP53-R213*, PIK3CA-E545K) were grown
139 in NOD-Cg-Prkdcscid Il2rgtm1Wjl/SzJ mice (Jackson Laboratory, Bar Harbor, ME, USA), also
140 known as NOD SCID gamma (NSG). Tumors were grown in donor mice to a volume of

141 ~1500mm^3, harvested rapidly after euthanasia, cut into 2×2×2 mm^3 pieces under sterile
142 conditions, and surgically implanted into the left flank. Surgical staples were removed about ten
143 days post implantation, and tumor growth and mouse weight were measured twice per week. At
144 the average tumor volume of 100mm^3, mice were randomized and treated as described above.

145 **Complete Blood Counts**

146 Blood was collected by cardiac puncture into a tube containing EDTA to prevent coagulation at
147 the endpoint of the study. The analysis was performed using the HemaTrue Analyzer and
148 HeskaView Integrated Software version 2.5.2. Graphs for the blood compounds were generated
149 using GraphPad Prism8 (Version 8.4.2).

150 **Immunoblotting**

151 Whole-cell lysates were prepared using NP40 Lysis Buffer (0.88% NP-40, 132 mM NaCl, 44
152 mM HEPES, and 8.8 mM NaF) supplemented with 2 mM sodium orthovanadate, 1 mM PMSF,
153 and Protease Inhibitor Cocktail. Protein concentrations were quantified using the Bio-Rad DC
154 Protein Assay (Cat# 5000111). Equal amounts of protein from each sample were heated for 5
155 min and resolved by SDS-PAGE at a constant voltage of 100V. Proteins were then transferred
156 onto a nitrocellulose membrane (0.2-µm pore size) at a constant voltage of 100V for 120 min at
157 4°C. Membranes were blocked in 1x TBS-T (Tris-buffered saline (TBS)) with 0.1% v/v
158 TWEEN-20) and 5% w/v non-fat dry milk. Primary antibodies were diluted in 5% BSA or 5%
159 milk in 1x TBS-T and incubated overnight at 4°C. The membranes were washed three times with
160 1x TBST for 10 min each and then incubated with secondary mouse or rabbit HRP-conjugated
161 antibody for 1h at room temperature. The membranes were washed three times with 1x TBST for
162 15 min each. Pierce ECL Western Blotting Substrate was used for chemiluminescent detection.
163 Signals were visualized and imaged using radiographic films.

164 **Cell cycle analysis by Flow Cytometry**

165 Cells were seeded at 300,000 cells/well in 6-well plates and then treated for 24h with various
166 concentrations of drugs, listed in **Key Resources Table**. Cells were collected and fixed with ice-
167 cold 70% ethanol for 1h at -20°C and stained for 1h at 4°C in Krishan DNA Buffer (propidium
168 iodide, sodium citrate, RNase A, NP40, and 0.1 mM HCl). The samples were analyzed on a BD
169 LSR Fortessa cytometer running FACS Diva (version 6.1.3), and the data were processed using
170 FCS Express 7 (version 7.06.0015). The experiments were repeated twice, and representative
171 histograms are shown.

172 **Cytotoxicity**

173 The cells were seeded at a density of 5,000 cells/well in a 96-well plate. After 24h, cells were
174 treated with TAS102 at a range of concentrations in the presence of 100nM talazoparib, and/or
175 the G2 kinase inhibitors at various concentrations for 72h. The cells were stained with 1%
176 methylene blue for 30 min, rinsed with water, and dried overnight. The cells were solubilized in
177 5% SDS prepared in PBS, and absorbance was measured at 650 nm. IC50 values were calculated
178 using GraphPad Prism (version 10.0.3). Combination Index (CI) values were calculated based on
179 the Loewe Additivity Model as implemented in the SynergyFinder R package using the
180 following formula: $CI = D1/IC50_1 + D2/IC50_2$, where D1 and D2 are the concentrations of drugs
181 1 and 2 used in the combination, while $IC50_1$ and $IC50_2$ are the concentrations of drugs 1 and 2
182 inhibiting 50% of the activity when used individually. Each dot in the Scatter plot represents the
183 drug interaction in the combination at specific concentrations, plotted against the fraction
184 affected (Fa). The CI values are distributed below, at, or above the threshold of 1, indicating
185 synergy ($CI < 1$), additivity ($CI = 1$), or antagonism ($CI > 1$).

186 **Immunohistochemistry (IHC)**

187 Freshly isolated tumors were fixed in 10% neutral buffered formalin (Sigma-Aldrich, Cat.
188 #HT501128) for 48h, then transferred to 70% ethanol for dehydration, before embedding in

189 paraffin at Roswell Park's Pathology Network Shared Resources (PNSR) into formalin-fixed
190 paraffin-embedded (FFPE) blocks. Staining for hematoxylin & eosin (H&E) and for p-Y15-
191 CDK1, Cyclin B1, and p-S10-HH3 was performed by the PNSR. Antibodies and reagents are
192 listed in **Key Resources Table.** Slides were scanned by Aperio ImageScope version 12.4.0.5043,
193 and representative images were captured at 20x magnification. Three representative tumors from
194 each treatment group were used for quantification. A minimum of eight fields of view (FOV)
195 were analyzed for each tumor sample. Entire stained tissue sections were scanned, and the areas
196 of highest density for immunoreactivity ("hot spots") were manually selected for quantification.
197 Each "hot spot" was recorded at 20x magnification. The positive area was calculated using the
198 formula: Negative area – Positive area × 100) in ImageJ. Data were reported as mean and
199 standard error (mean +- SE). Data are presented using GraphPad Prism8 (v8.4.2).

200 **Annexin-V staining**

201 Following drug exposure, the cells were trypsinized, washed with PBS, and resuspended
202 in annexin-binding buffer. Dead cells were stained for annexin-V and DNA with propidium
203 iodide according to the manufacturer's instructions (Dead Cell Apoptosis Kit with Annexin-V-
204 FITC and PI, for flow cytometry, ThermoFisher Scientific, Cat. No.: V13242). The samples were
205 processed on a BD LSR Fortessa cytometer running FACS Diva (v6.1.3), and the data were
206 analyzed using FCS Express 7 (v7.06.0015). Experiments were repeated twice, and
207 representative histograms were shown.

208 **Immunofluorescence microscopy**

209 The cells were grown on glass coverslips for 24h and then treated with 500nM TAS102, 100nM
210 talazoparib, or their combination for the indicated time; alternatively, cell were treated with
211 TAS102-talazoparib for 25h following drug withdrawal in incubation for indicated time. Cells
212 were fixed with 4% PFA and permeabilized with 0.05% Triton X-100. Samples were blocked

213 with 3% milk in PBS and probed with γH2AX and RAD51 antibodies in 1% milk, followed by a
214 wash in PBS and incubation with fluorescent secondary antibodies in 0.5% milk. Samples were
215 washed with PBS three times and DNA was labeled with Hoechst 33342 before mounting on
216 glass slides. Fluorescence images were taken with a Plan Apochromat 100x objective (1.40 NA
217 mineral oil) at ambient temperature using a Nikon TE2000-E inverted microscope equipped with
218 a charge-coupled device camera (CoolSNAP HQ; Photometrics). The levels of γH2AX and
219 RAD51 were assessed by measuring cellular fluorescence intensity as the Corrected Total
220 Cellular Fluorescence (CTCF). Briefly, a minimum of six random fields per treatment group
221 were evaluated using MetaVue imaging software (version 7.7.3, Molecular Devices). Three
222 background readings were measured for each field of view and individual cells that were
223 positively stained with γH2AX and RAD51 were selected with a region freehand tool. For each
224 treatment group, >40 cells were evaluated and the CTCF values were calculated using the
225 formula: integrated density – (area of cell × average background fluorescence). The CTCF values
226 are reported as mean and standard error (mean +- SE). Data are presented using GraphPad
227 Prism8 (v8.4.2).

228 **RNA sequence**

229 Cells were seeded at a density of $1x10^6$ cells in a 100mm dish, and the following day media was
230 replaced with base media containing 5% FBS for 6h. Cells were then treated with 500nM
231 TAS102, 100nM talazoparib or their combination for 24h. Next day, cells were lysed with
232 TRIzol reagent (Thermofisher Scientific; Cat # 15596026). RNA was isolated using Direct-zol
233 RNA Miniprep Kit (Zymo Research; Cat # R2050). The sequencing libraries are prepared from
234 500ng total RNA using the mRNA HyperPrep kit (Roche) and following manufacturer's
235 instructions. The polyA+ RNA population was captured using the mRNA Capture Beads and

236 then utilized for cDNA synthesis using random primers and reverse transcriptase. cDNA was
237 converted into blunt-ended double-strand DNA using Taq pol (overhanging A) and purified
238 using Pure Beads (Roche). Multiple indexing adapters with overhanging T at the 3' end were
239 ligated to the ds-cDNA ends. Adapter ligated ds-cDNA libraries were amplified by PCR,
240 purified using Pure Beads, and then were validated for appropriate size on a 4200 TapeStation
241 D1000 Screentape (Agilent Technologies, Inc.). The DNA libraries were quantitated using
242 KAPA Biosystems qPCR kit, and were pooled together in an equimolar ratio, following
243 experimental design criteria. Each pool was denatured and diluted to 200pM with 1% PhiX
244 control library added. The resulting pool was then loaded into the appropriate NovaSeq Reagent
245 cartridge, as determined by the desired sequencing depth and number of samples. 100-cycle
246 paired-end sequencing was then performed on a NovaSeq6000 following the manufacturer's
247 recommended protocol (Illumina Inc.).
248 Raw count files were generated from FASTQ files using UB CCR's HPC nr-core/rnaseq pipeline
249 (https://nf-co.re/rnaseq/3.12.0). Raw sequencing reads passed quality filters from Illumina RTA
250 were first pre-processed by using FASTQC (v0.11.8) for sequencing base quality control. The
251 reads were mapped to GRCh38 human reference genome and the GENCODE (v38) (128)
252 annotation database using STAR (v2.7.9a). Counts from RSEM were filtered and then upper
253 quartile normalized using R package edgeR. Gene Ontology analysis of biological processes
254 pathways was selected based on adjusted p-values, and the NES was calculated by ranking all
255 genes based on their differential expression, calculating the Enrichment Score (ES) for each gene
256 set, and normalizing the ES by dividing it by the mean ES values from random permutations.
257 Cell-cycle genes in the heatmap were derived from the Cyclebase 3.0 database.
258 **Quantification and Statistical Analysis**

259 Statistical analysis was performed using GraphPad Prism software (v10.0.3) unless otherwise
260 indicated. The data represent biological replicates (n) as mean value with standard error (mean ±
261 SE). Statistical significance of data comparisons was determined using the Student's unpaired *t*-
262 test with a two-tailed distribution, one way ANOVA, or two-way ANOVA with a Tukey
263 multiple comparisons test or with Sidak's multiple comparisons test as indicated in figure
264 legends. Statistical significance was achieved when $P<0.05$. The correlation analysis was
265 performed using the Pearson correlation approach in RStudio. Survival was evaluated using the
266 Kaplan-Meier estimator with the log-rank test, based on time-to-arrive at a defined tumor volume
267 using GraphPad Prism. Cytotoxicity data were normalized to that of the control, and IC50 values
268 were calculated using three-parameter nonlinear regression.
269

270 **RESULTS**

271 **The TAS102-talazoparib treatment activates DNA damage response and arrests cells in G2.**

272 Prior studies have shown that the incorporation into DNA of thymidine analogs (i.e., ethynyl-
273 deoxyuridine, EdU, or trifluorothymidine, a component of TAS102) triggers post-replicative
274 repair, resulting in single-strand DNA break (SSB) intermediates [17, 18]. The addition of a PARP
275 inhibitor (PARPi) greatly increases the formation of double-strand breaks (DSBs) [17, 18]. DNA
276 damage activates the p53-dependent G1 checkpoint and DNA repair in non-tumor p53WT cells,
277 whereas p53mut cells (exhibiting a compromised G1 checkpoint) accumulate DSBs and respond
278 with the G2 checkpoint [17, 18]. To define the molecular mechanisms of the G2 checkpoint response
279 to TAS102-PARPi treatment, isogenic CRC cell lines with p53WT, p53mut or p53- deletion
280 (KO, knockout) were utilized. Treatment with talazoparib (PARPi) for 24h increased the G2
281 population in p53mut and p53KO cells but had little effect on p53WT cells, whereas TAS102

282 alone increased the G2 population in p53mut/p53KO cells and a moderate G2 increase in p53WT
283 cells (**Fig. 1a-b**). TAS102-talazoparib treatment (TAS-Tal) exerted in p53mut/p53KO cells a
284 strong increase in the G2 population and a reciprocal decrease in the G1 population, and these
285 changes were statistically significant (**Fig.1a-b**). In p53WT cells, the combination did not
286 increase the G2 population compared to TAS102 alone. Immunoblot analysis of cell cycle and
287 DNA damage response (DDR) markers showed that TAS102 and TAS102-PARPi decreased the
288 activating phosphorylation of PLK1, a kinase mediating mitotic transition, independent of p53
289 status (**Fig.1c-d**). TAS102-PARPi treatment increased an inactivating phosphorylation of CDK1
290 at Tyr15 (**Fig. 1c-d**), a site known to be phosphorylated by WEE1 kinase. Protein levels of
291 cyclins A2 and B1, partners of CDK1, were also elevated (**Fig.1c-d**). In contrast,
292 phosphorylation of histone H3 was not increased, indicating no entry into mitosis (**Fig.1c-d**).
293 Together, these results showed induction of the G2 checkpoint and DDR in p53-deficient cells
294 upon treatment with TAS102 alone and more robustly in combination with PARPi (**Fig.1g**). To
295 validate this observation *in vivo*, the G2 markers were examined by immunohistochemistry
296 (IHC) in tumor tissues from the CRC PDX models (generated within the Phase I clinical
297 NCT04511039 study), which were treated with vehicle or drugs (talazoparib, TAS102, or
298 combination) as described [18]. IHC analysis showed that TAS102 and TAS102-PARPi increased
299 the levels of phospho-Tyr15-CDK1 and Cyclin B1 in $p53^{H179R}$ mutant model (PDX-02-07-RP),
300 whereas the levels of phospho-H3 were reduced (**Fig. 1e** and **Suppl. Fig.1a-b**). Similar results
301 were obtained in the PDX-01-03-RP model carrying p53WT, although the effects of the drug
302 combination were lower in the p53WT model (**Fig. 1f** and **Suppl. Fig.1c-d**). These findings
303 indicate that the TAS102-PARPi combination primarily activated the G2 checkpoint in p53mut
304 cancers, while p53WT cells responded by activating both G1 and G2 checkpoints (**Fig. 1g)**.

305

306 **TAS102-talazporib alters the transcriptomic program in p53WT and p53mut cells.**

307 To better define the response to the two-drug combination, transcriptomic analysis was
308 performed on isogenic HCT116 p53WT and p53KO cell lines treated with drug monotherapies
309 or their combination for 24h. Talazoparib alone induced minimal transcriptomic changes in both
310 cell lines (**Fig. 2a, d**). In contrast, TAS102 exerted strong effects by inducing expression of 774
311 genes and downregulating expression of 367 genes in p53WT cells and 614 upregulated and 418
312 downregulated genes in p53KO cells relative to vehicle-treated controls (**Fig. 2b, e**). The drug
313 combination in p53WT cells increased expression of 897 genes and decreased expression of 368
314 genes, while in p53KO cells expression of 698 genes was induced and that of 615 genes was
315 decreased (**Fig. 2d, f**). The Venn diagrams demonstrated a notable overlap in altered gene
316 expression between TAS102 monotherapy and the TAS102-PARPi combination, with 936 genes
317 shared in p53WT and 770 shared in p53KO cells (**Fig. 2g-h**).

318 The gene ontology (GO) enrichment analysis was conducted on the differentially expressed
319 genes (**DEGs**) to infer the biological processes affected by the drug treatments. The GO analysis
320 showed that in both p53WT and p53KO cells treated with TAS102, the up-regulated genes were
321 enriched in processes associated with cell cycle regulation and extracellular matrix (ECM)
322 organization (**Suppl. Fig. 2a-b**). However, among the downregulated genes distinct processes
323 were affected in p53WT *vs*. p53KO cells. In p53WT cells, downregulated genes were mainly
324 associated with processes related to mRNA splicing and pyrimidine metabolism, whereas in
325 p53KO cells with processes related to ribosome biogenesis, rRNA processing and maturation
326 (**Suppl. Fig. 2a-b**). In TAS102-talazoparib treatment, the top upregulated biological processes in
327 p53KO cells were related to DNA replication and G2/M transition, whereas downregulated

328 processes were related to ribosome biogenesis (**Suppl. Fig. 2c-d**). The dot plots summarize the
329 top significantly enriched processes related to cell cycle regulation, ECM organization, and
330 ribosome biogenesis for p53WT and p53KO cells (**Fig. 2i**). The upregulation of processes related
331 to ECM organization suggests a contribution of the matrix to cell division, while repression of
332 ribosome biogenesis is consistent with reduced ribosome biogenesis at the G2 checkpoint in
333 preparation for mitosis [20].

334 To reveal the transcriptome changes related to the cell cycle and DNA repair in p53WT *vs*.
335 p53KO cells, heatmaps were built for p53 targets, cell cycle, and DNA repair genes identified in
336 the GO analysis. The regulation of p53 target genes was clearly different between p53WT and
337 p53KO cells (**Fig. 2j, k**). Treatment of p53WT cells with TAS102 (TAS) or TAS102-PARPi
338 (TAS+Tal) strongly induced the expression of p53 targets (i.e., p21/CDKN1A, MDM2, BTG2);
339 in contrast their regulation was markedly lower in p53KO cells (**Fig. 2j, k**, p53 Targets). In
340 p53KO cells the expression of homologous recombination (HR) DNA repair genes (i.e., BRCA1,
341 BRCA2, RAD51) was robustly induced by TAS102-PARPi treatment, whereas the effect was
342 lower in TAS102 alone (**Fig. 2j, l**, HR genes). This finding is consistent with higher double-
343 strand breaks (DSBs) induced by TAS102-PARPi treatment in p53KO cells compared to
344 TAS102 alone [17, 18]. The genes involved in G1/S transition (CDK4, E2F1, E2F3) and DNA
345 replication (MCM6, PRIM2) were reduced in p53WT cells treated with TAS102 and TAS102-
346 PARPi (**Fig. 2j, m**). In contrast, treatment of p53KO cells with TAS102 or TAS-PARPi
347 increased the expression of genes mediating G1->S transition (E2F1, E2F3, TFDP1) and DNA
348 replication (CCNE1, CDK2, MCM10, ORC1), **Fig. 2j, m**, G1/S and S/G2 genes. These effects
349 show that neither TAS102 nor TAS-PARPi repress DNA replication in p53-deficient cells,
350 whereas the treatments of p53WT cells induce a p53-dependent G1-arrest. Importantly, TAS-

351 PARPi treatment of p53KO cells strongly reduced expression of genes involved in mitosis
352 (AURKA, BUB1, CDC20, CENPF, PLK1, PIF1), an effect that was lower in TAS102 alone
353 (**Fig. 2j**, **n**, M phase). In contrast, the expression of these genes was not reduced in p53WT cells.
354 We further verified the transcriptome effects in the HT29 CRC cell line carrying $p53^{R273H}$.
355 RNAseq analysis showed that TAS102-PARPi treatment downregulates expression of M-phase
356 genes and upregulates expression of HR-related genes comparable to the effects observed in
357 HCT116-p53KO cells (**Suppl. Fig. 3**). The TAS102-PARPi effects were greater than those of
358 TAS102 alone. Together, these data showed that the TAS102-PARPi treatment caused distinct
359 transcriptome changes in p53-deficient *vs*. p53WT cells, consistent with G2-arrest and activation
360 of HR-mediated DSB repair in p53mut cells and G1-arrest in p53WT cells.
361

362 **Targeting G2 checkpoint kinases and cytotoxicity of TAS102-PARPi treatment.**

363 We have shown that TAS102-PAPRi treatment activates signaling by ATM and ATR kinases
364 [18], which are known to mediate DNA repair and G2-arrest [21, 22]. Therefore, we examined whether
365 blocking these kinases can enhance the toxicity of TAS102-PARPi in p53mut cells. A selective
366 ATM inhibitor (KU55933; ATMi) did not enhance toxicity of TAS102-talazoparib in p53WT
367 and p53-deficient (p53KO, $p53^{R248W/-}$) HCT116 cell lines (**Suppl. Fig. 4a-c**). Instead, ATMi
368 reduced sensitivity to TAS102-talazoparib in all tested lines, potentially due to ATM function in
369 the G1/S checkpoint [23] and/or recovery of replication fork after DNA repair [21, 22]. In contrast, the
370 selective ATR inhibitor (AZD6738/ceralasertib; ATRi) markedly enhanced toxicity of TAS102-
371 talazoparib in p53KO and p53mut cell lines (**Fig. 3a-d**). In p53-deficient cells the IC50 was
372 enhanced 4-10-fold by 100nM ATRi (**Fig. 3b-d, n**), whereas only 1.5-fold increase was observed
373 in p53WT cells (**Fig. 3a, n**). This result is consistent with our prior finding that, in cells treated

374 with TAS102-talazoparib, blockade of ATR increases levels of γH2AX (a DNA damage marker)
375 [18]. Furthermore, blockade of ATR, but not ATM, increased phosphorylation of histone H3
376 (phospho-H3, a marker of mitosis) (**Suppl. Fig.4i**). These data are aligned with the role of ATR
377 in resolving replication stress and activating the G2/M checkpoint, thus ensuring proper cell
378 cycle progression and DNA repair [24]. ATR kinase blockade allows cells with unrepaired DSBs to
379 enter mitosis, leading to cell death [22].

380 ATR kinase induces G2-checkpoint through downstream effector kinases such as CHK1 and
381 WEE1; CHK1 kinase phosphorylates and inactivates CDC25 phosphatase, which controls
382 CDK1, while WEE1 kinase inactivates CDK1 by phosphorylating Tyr15 [21, 25-30]. Therefore, we
383 explored whether blockade of these kinases would result in cytotoxic effects comparable to those
384 of ATRi. A selective CHK1 inhibitor (AZD7762; CHK1i) showed comparable increase in
385 cytotoxicity of TAS102-talazoparib in both p53WT and p53-deficient cells, about 8-10-fold at
386 100nM CHK1i (**Fig. 3e-i**). In contrast, a WEE1 inhibitor (MK1775; WEE1i) enhanced the
387 cytotoxicity of TAS102-talazoparib preferentially in p53mut cells, 8-15-fold in p53mut *vs* 3-4-
388 fold in p53WT cells at 100nM WEE1i (**Fig. 3j-m, o**).

389 Next, we examined the cytotoxicity of G2-kinase inhibitors in non-tumor p53WT MCF10A
390 cells. ATRi and WEE1i showed only a moderate (2-3-fold) enhancement of toxicity of TAS102-
391 talazoparib in non-tumor cells (**Suppl. Fig. 4d, f**). In contrast, CHK1i strongly enhanced toxicity
392 of TAS102-talazoparib (nearly 10-fold) in non-tumor cells (**Suppl. Fig. 4e**). Immunoblotting
393 verified the activities of CHK1 and WEE1 inhibitors on DNA damage response (DDR) markers
394 in p53WT MCF10A and p53mut MDA-MB-231 cells (**Suppl. Fig. 4g, h**). Consistent with the
395 effects of CHK1i *in vitro*, clinical trials have shown significant toxicities associated with CHK1i,
396 resulting in discontinued early trials [31, 32]. Conversely, drugs targeting ATR and WEE1 have

397 shown tolerable toxicity in clinical trials [33, 34], positioning them as potential therapeutic
398 candidates. Given that efficacy of TAS102-talazoparib was enhanced by both ATRi and WEE1i
399 preferentially in p53mut cells, we evaluated the drug interaction using the Loewe Additivity
400 Model [35, 36]. The analysis revealed synergism between TAS102-talazoparib and both ATRi and
401 WEE1i in p53mut cell models, with cooperativity index (CI) values ranging from 0.21 to 0.30
402 for ATRi (**Fig. 3n**, **Suppl. Fig. 5a-d**) and 0.16-0.30 for WEE1i (**Fig.3o**, **Suppl. Fig. 5f-i**). In
403 contrast, in non-tumor p53WT cells, ATRi and WEE1i did not show substantial cooperativity
404 with TAS102-talazoparib with the CI values of 0.73 and 0.69, respectively (**Fig. 3n-o** and **Suppl.**
405 **Fig. 5e, j**). Thus, in this simultaneous drug regimen, TAS102-talazoparib synergized with ATRi
406 and WEE1i in p53mut cancer cells, while exerting only a moderate interaction in p53WT cells.
407

408 **TAS102-talazoparib induces persistent DNA damage in p53-mutant cancer cell models.**

409 A clinical drug regimen for TAS102 and TAS102-talazoparib includes cycles of 5-days On-
410 treatment plus a 9-day Off period [37]. To explore the response dynamics, the cell-cycle analysis
411 was performed on p53WT and p53-deficient cells treated with TAS102-talazoparib followed by
412 drug washout. In p53WT cells, an increase in the G2 population was observed following the two-
413 drug treatment and remained elevated up to 24h after drug washout, then followed by a gradual
414 increase in the G1 population, with a small fraction of sub-G1 cells (**Fig. 4a**). In contrast, p53KO
415 and p53R248W cells responded to TAS102-talazoparib with a prolonged G2-arrest even after
416 drug withdrawal. Moreover, the sub-G1 population was increased at 48-72h after drug
417 withdrawal, indicating cell death in p53-deficient cells (**Fig. 4b-c**).

418 To verify the cell cycle effects and to assess DNA damage, the molecular markers of DDR
419 and cell cycle were examined by immunoblotting in cells treated with TAS102-talazoparib for

420 24h followed by drug washout. In HCT116-p53WT cells, 24h-treatment with TAS102-
421 talazoparib (T0) induced the markers of G2-checkpoint (phospho-CHK1 and phospho-CDK1)
422 and DNA damage (γH2AX) (**Fig. 4d**). The levels of these markers decreased after 24hours of
423 drug washout. Protein levels of p21/CDKN1A (a p53 target) followed this trend with a reduction
424 at 36h (**Fig. 4d**). Cyclin D1 levels increased at 36h, indicating a recovery of cell cycle capacity
425 (**Fig. 4d**). Together, these findings align with the cell cycle data (**Fig. 4a**). In contrast, HCT116-
426 p53KO and HCT116-p53$^{R248W/-}$ cells exhibited sustained phospho-CHK1, phospho-CDK1, and
427 γH2AX levels after the TAS102-talazoparib treatment, indicating a prolonged G2-arrest with
428 high DNA damage (**Fig. 4e-f**). Consistent with this, cyclin D1 protein levels remained low, not
429 recovering within 72h (**Fig. 4e-f**). Comparable results were observed in HT29-p53^{R273H} cells
430 (**Fig. 4g**), where a prolonged increase in DNA damage and G2 markers mirrored the data in
431 HCT116 p53KO and p53R248W/- cell lines.

432 To validate the recovery of cell proliferation following treatment with TAS102-talazoparib
433 for 24h and drug withdrawal, cell growth was examined using live-cell imaging. The analysis
434 showed that p53WT non-tumor MCF10A cells quickly recovered growth capacity after drug
435 washout, while growth recovery was delayed by ~48h in p53WT HCT116 cells (**Suppl. Fig. 6a,**
436 **b**). In contrast, p53KO and p53mut cancer cells did not regain the growth capacity within the 92h
437 timeframe of the experiment (**Suppl. Fig. 6c-d**).

438 Together, these data showed that TAS102-talazoparib induced in p53-deficient cells a long
439 G2-arrest and persistent DNA damage observed even after 72h of drug withdrawal, and a sizable
440 proportion of p53mut cells underwent cell death within 48-72h (sub-G1 fraction). In contrast,
441 p53WT cells were able to repair DNA and recover their cell cycle capacity within 48h of drug
442 withdrawal.

443

444 **The dynamics of DNA repair following TAS102-talazoparib treatment in p53mut cells**

445 To evaluate the dynamics of DNA damage repair, changes in the DSB markers γH2AX and
446 RAD51 were examined in MCF10A (p53WT), DLD1 ($p53^{S241F}$), and HT29 ($p53^{R273H}$) cell lines
447 using immunofluorescence. Cells were treated with TAS102-talazoparib for 24h followed by
448 drug washout. Immediately after 24h-treatment (at T0), the levels and the foci formation of
449 γH2AX and RAD51 were increased in all tested cell lines (**Fig. 5a, d, e, g, j, k, m, n**). In
450 MCF10A cells, the nuclear area was increased by nearly 2-fold (from 130μm^2 to 250μm^2)
451 (**Fig.5c, f**), indicating enlargement of the nucleus in a significant proportion of cells (about 77%
452 with area of 200-580μm^2, insert). Following drug withdrawal, the γH2AX and RAD51 signals
453 and the nuclear sizes were decreased within 24-48h in MCF10A cells (**Figs. 5c-f**). These data
454 show that DNA damage by TAS102-talazoparib was repaired, and cells completed the mitotic
455 cell division. In contrast, the γH2AX/RAD51 signals were not reduced in p53mut DLD1 and
456 HT29 cell lines within 72h of drug washout (**Fig. 5g-h, j-k, m-n**). The nuclear area was also
457 increased at T0, and a sustained enlargement was observed at 24-48h of drug washout (**Fig. 5i, l,**
458 **o**). These results indicate that p53mut cells replicate DNA but do not undergo cell division
459 resulting in enlarged nucleus, and DSBs are not repaired up to 72h of drug washout. Together,
460 these observations show that the TAS102-PARPi treatment can induce DNA breaks and G2-
461 arrest in p53WT and p53mut cells. However, DNA repair and recovery of cell division were
462 remarkably different in p53WT and p53mut cells. Non-tumor p53WT cells repaired DNA breaks
463 and completed the mitotic cell division within 48h, whereas p53mut cells could not complete
464 DNA repair and cell division, resulting in high levels of DNA breaks and G2-arrest even at
465 72hours of drug withdrawal. These observations are aligned with the cell cycle and cell growth

466 data, which showed a lack of proliferation in p53mut cells within this timeframe (**Fig. 4, and**
467 **Suppl. Fig.5**). Thus, TAS102-PARPi treatment induced high DSB levels and long G2-arrest in
468 p53mut cancer cells, while p53WT cells repaired DNA and recovered cell cycle capacity.
469

470 **A sequential triple-drug approach using TAS102-PARPi treatment followed by blockade of**
471 **WEE1 kinase elicits synergistic toxicity in p53mut cancer cells.**

472 TAS102-PARPi treatment induced DNA breaks and sustained G2-arrest in p53mut cells even
473 after drug washout, whereas non-tumor p53WT cells recovered remarkably faster (**Figs. 4-5**).
474 Next, we examined whether toxicity of TAS102-PARPi treatment in p53mut cells can be further
475 enhanced by blockade of a G2-checkpoint kinase. Cells were treated with TAS102-talazoparib
476 for 24h, followed by drug washout for 24h and subsequent incubation with WEE1i (MK1775)
477 for 48h. Cytotoxicity assays showed that WEE1i did not synergize with TAS102-PARPi in
478 p53WT MCF10A cells, ~1.1-fold at 100nM WEE1i (**Fig. 6a, f**). In HCT116-p53WT cells,
479 WEE1i only modestly enhanced the IC50 of TAS102-talazoparib (by ~1.4-fold at 100nM
480 WEE1i). In contrast, in HCT116-p53KO and HCT116-p53^{R248W} cell lines WEE1i at 100nM
481 enhanced toxicity of TAS102-talazoparib by ~3.6-fold and ~2.5-fold, respectively (**Fig. 6b-d, f**).
482 In HT29 (p53^{R273H}) cells, the toxicity of TAS102-talazoparib was enhanced by ~7-fold at 100nM
483 WEE1i (**Fig. 6e-f**). Evaluation of drug interactions in this sequential regimen showed CI = 0.94
484 for MCF10A cells and CI = 0.57 for HCT116 cells (both p53WT), indicating no or modest drug
485 interactions (**Fig. 6f**). In contrast, p53-deficient cells, HCT116-p53KO or p53mut cells
486 (HCT116-p53^{R248W} and HT29-p53^{R273H}), showed CI values ranging 0.26-0.42, indicating a
487 synergistic interaction between TAS102-talazoparib and WEE1i (**Fig. 6f**).

488 Examination of cell death, using flow cytometry with Annexin V and propidium iodide (PI)
489 staining, showed that the sequential treatment of MCF10A cells with TAS102-PARPi followed
490 by 100nM WEE1i resulted in ~9% double-positive (annexin-V^+/PI^+) dead cells, compared to
491 ~8% dead cells by TAS102-PARPi treatment alone (**Fig. 6g-h**). In HCT116-p53WT cells, ~19%
492 of cells were double-positive after TAS102-talazoparib treatment and ~39% after the sequential
493 triple-drug combination (**Fig. 6g, i**). Approximately 29% of HCT116-p53KO cells were double-
494 positive in response to TAS102-talazoparib, and cell death increased to ~68% after triple-drug
495 treatment (**Fig. 6g, j**). In HT29 cells, TAS102-talazoparib treatment resulted in ~30% double-
496 positive cells, whereas the sequential drug combination resulted in ~76% double-positive dead
497 cells (**Fig. 6g, k**). Similar effects of a sequential triple-drug treatment were observed in p53mut
498 MDA-MB-231 cells compared to p53WT MCF10A cells (**Suppl. Fig. 7**). Together, these data
499 showed a synergistic toxicity of TAS102-talazoparib treatment followed by WEE1i in p53mut
500 cancer cells, whereas this sequential triple-drug regimen showed low toxicity in non-tumor
501 p53WT cells.
502

503 **Anti-tumor efficacy of the sequential triple-drug combination**

504 The therapeutic efficacy of the sequential combination of TAS102-talazoparib and WEE1i
505 was examined in tumor xenograft models. The drug regimen included repeats of the two-week
506 cycle with TAS102-talazoparib treatment in the first week followed by WEE1i treatment in the
507 second week, based on the clinical schedule for TAS102 and TAS102-talazoparib [37]. This two-
508 week regimen was initially tested in xenografts of HT29 cells ($p53^{R273H}$, $BRAF^{V600E}$) in SCID
509 mice. Treatment was initiated when tumors reached $100mm^3$ using 5-days-ON, 2-days-OFF
510 schedule in four groups: vehicle, WEE1i (every week), TAS102-talazoparib (every week), and

511 the triple-drug combination (a sequential two-week cycle). Treatment with WEE1i had a limited
512 effect on tumor growth with tumor growth inhibition (TGI) of 18%, whereas TAS102-
513 talazoparib was more effective, with a TGI of 43% (**Fig. 7a-b**), consistent with our previous
514 studies[18]. Importantly, a sequential combination of TAS102-talazoparib and WEE1i showed
515 greater tumor growth control than each treatment alone, with a TGI of 63% (**Fig. 7a-b**). The
516 triple-drug regimen also improved survival to 39 days compared to 32 days for TAS102-
517 talazoparib, and 24 days for WEE1i alone (**Fig. 7c**). Neither treatment affected animal weight
518 compared to the control group (**Fig.7d**), indicating the absence of major toxic side effects.
519 The efficacy of the triple-drug regimen was tested in a patient-derived xenograft (PDX)
520 model (PDX-3B1-29-RP, $p53^{R213*}$) established from a colorectal cancer biopsy within the
521 clinical trial NCT04511039. The R213* truncating p53 mutation is commonly found in human
522 tumors and exhibits pro-tumor effects [38]. Treatment with TAS102-talazoparib reduced tumor
523 growth by ~20% and WEEi1 alone had no effect, whereas the sequential drug combination
524 reduced tumor growth by ~50% (**Fig. 7e-f**) and extended survival from 24 to 43 days (**Fig. 7g**).
525 No major toxic side effects by the treatments were noted based on the examination of mouse
526 weight (**Fig.7h**), the bone marrow histology, and peripheral cell blood counts (**Suppl. Fig. 8**).
527 The efficacy was further examined in a pancreatic cancer PDX model (PDX-14312-5p) carrying
528 $p53^{R175H}$ and $KRAS^{G12R}$ mutations. It was observed that WEE1i monotherapy modestly reduced
529 tumor growth (~30%), whereas TAS102-talazoparib was more effective in tumor control, with a
530 TGI of ~43% on day 50 (**Fig.7i-j**). The triple-drug regimen showed remarkably greater tumor
531 control than either treatment alone (TGI ~80%, **Fig.7i-j**) and extended survival to >75days,
532 compared to ~64 days by TAS102-talazoparib and 48 days by WEE1i (**Fig.7k**). No major
533 toxicity signs were noted based on mouse weight (**Fig.7l**). Together, these data demonstrate that

534 the triple-drug regimen combining the two-drug TAS102-PARPi treatment followed by WEE1i
535 is effective against p53mut cancer models and the regimen is well tolerated in mice.
536

537 **DISCUSSION**

538 Treatment of p53mut cancers remains a significant clinical challenge mainly due to lack of
539 effective therapeutic options [9, 10]. Here, we introduce a triple-drug strategy for p53mut cancers
540 combining two-drug TAS102-PARPi treatment with blockade of the G2-checkpoint. TAS102-
541 PARPi treatment acts as an *inducer-amplifier* pair to induce DNA double-strand breaks (DSBs)
542 and G2-arrest selectively in p53mut cancer cells. Subsequent blockade of the G2-checkpoint
543 kinase WEE1 releases G2-arrested cells into mitosis leading to cell death, acting as a *terminator*.
544 We found that delaying WEE1i application until after TAS102-PARPi treatment allows normal
545 p53WT cells to repair their DNA, thus reducing the impact on normal cells (**Figs. 5-6**). This
546 sequential triple-drug approach is a promising therapeutic strategy for treatment of p53mut
547 cancers as it showed high efficacy in preclinical cancer models and was well tolerated in mice.
548 Prior work has shown that TAS102-PARPi treatment induces high levels of DNA damage in
549 p53mut cancer cells, and this effect was linked to a compromised G1/S checkpoint [17, 18].
550 Thymidine (dT) analogs, such as trifluorothymidine (TFT, a component of TAS102) or ethynyl-
551 deoxyuridine (EdU), are incorporated into DNA during replication[17, 18]. These dT-analogs also
552 inhibit thymidylate synthase[39], leading to the incorporation of uridine residues into DNA[17, 18, 40].
553 The incorporated analogs are removed from DNA by base-excision repair (BER) resulting in
554 single-strand breaks (SSBs) [17, 18, 40], which are repaired *via* a mechanism involving PARP1[41].
555 PARP1 inhibitors (such as talazoparib) compromise SSB repair, increasing levels of more lethal
556 DSBs that further activate DDR signaling mediated by ATM and ATR kinases. In p53WT cells,

557 DDR signaling mediated by ATM activates the p53-p21 axis resulting in G1-checkpoint
558 activation [18]. p21/CDKN1A inhibits CDK2 and CDK4/6 leading to cell cycle arrest in G1/S
559 and/or inhibit CDK1-cyclin B1 contributing to G2-arrest [42-44]. This effect of TAS102-PARPi
560 treatment is consistent with the role of ATM-CHK2-p53 signaling in DNA damage response [42,
561 43]. In p53mut cells with compromised G1/S checkpoint, TAS102-PARPi treatment resulted in
562 high DSBs and activation of the G2-checkpoint mediated by ATR (this study and [18]).
563 The distinct effects of TAS102-PARPi treatment on p53WT and p53-deficient cells were also
564 reflected in the transcriptomic program. In p53WT cells, TAS102-PARPi reduced expression of
565 genes involved in the G1/S transition (e.g., E2F1, E2F3), indicative of G1-arrest. However, in
566 p53-deficient cells, TAS102-PARPi increased expression of the G1/S transition factors (E2F1,
567 E2F3) and S/G2-phase genes (e.g., CCNE1, CCNE2, CDT1), consistent with the lack of G1/S
568 checkpoint in these cells. Moreover, TAS102-PARPi treatment reduced expression of M-phase
569 genes (i.e., AURKA, BUB1, CDC20, PLK1), consistent with G2-arrest in p53-deficient cells.
570 Thus, TAS102-PARPi treatment had distinct effects on p53WT and p53mut cells in the global
571 gene expression program related to cell cycle control.
572 Transcriptome analysis also revealed striking upregulation of HR-related DSB repair genes
573 (BRCA1, BRCA2, RAD51, RECQL, RBBP6) in p53-deficient cells. This distinct effect of
574 TAS102-PARPi treatment is likely to reflect DNA repair at the G2-checkpoint controlled by
575 ATR kinase [45]. ATM may also contribute to DNA repair by acting through H2AX (γH2AX),
576 RAD51, and BRCA1/2, thus promoting homologous recombination (HR) [46-48]. Thus, in addition
577 to G2-arrest, TAS102-PARPi treatment upregulated HR-mediated DNA repair.
578 Cytotoxicity studies showed a substantial dichotomy in the consequences of ATM and ATR
579 inhibition. Blockade of ATM reduced sensitivity to TAS102-talazoparib treatment in all tested

580 lines cells, independent of the p53 status. This effect of ATM blockade is likely related to the
581 function of ATM in the G1/S checkpoint [23] or replication fork recovery after DNA repair [21, 22]. In
582 contrast, ATR blockade greatly enhanced cytotoxicity of TAS102-talazoparib in p53mut cells,
583 and this effect is related to transition to mitosis with high DNA damage (elevated phospho-H3
584 and γH2AX levels). These results are consistent with the role of ATR in activation of the G2/M
585 checkpoint and in the control of replication completion before mitosis [24]. ATR can also control
586 an intrinsic S/G2 checkpoint, and the ATR blockade may deregulate the S/G2 transition allowing
587 early mitosis with under-replicated DNA and DNA damage [45]. Thus, ATR plays a critical role in
588 activation and control of the G2-checkpoint in p53mut cells treated with TAS102-PARPi,
589 making ATR a potential target to further enhance efficacy of TAS102-PARPi treatment.
590 To induce the G2 checkpoint, ATR activates downstream effector kinases, such as CHK1
591 and WEE1, which inactivate the CDC25-CDK1 axis that controls transition to mitosis [21, 25-30].
592 Here, we found that CHK1 blockade in combination with TAS102-PARPi treatment was
593 cytotoxic in both non-tumor p53WT and p53mut cancer cells (**Fig. 3**). This effect may reflect
594 CHK1 role in S-phase and explain high toxicities of CHK1 inhibitors observed in clinical trials,
595 leading to discontinuation of early trials [31, 32]. In contrast, WEE1 blockade enhanced toxicity of
596 TAS102-talazoparib preferentially in p53mut cells, while showing limited toxicity in non-tumor
597 models (**Fig.3**). This effect is consistent with the tolerable toxicities of WEE1i observed in early-
598 phase clinical trials [33, 34].
599 The drug response studies showed that the selectivity and efficacy of the drug combinations
600 can be enhanced in a sequential triple-drug regimen. TAS102-talazoparib treatment of p53mut
601 cancer cells resulted in prolonged G2-arrest and persistent DNA damage even at 72h after drug
602 washout with a sizable amount of cell death (**Figs.4-5**). In contrast, p53WT cells were able to

603 repair DNA and re-enter the cell cycle within 48h of drug withdrawal. Moreover, a 24h-delay in
604 WEE1i treatment after TAS102-talazoparib washout was still highly effective against p53mut
605 cells but was markedly less toxic to normal cells (**Fig.6**). This sequential triple-drug regimen
606 (TAS102-talazoparib plus 24h-delayed WEE1i) resulted in massive 80% cell death in p53mut
607 cancer cells, whereas cell death was not increased in non-tumor cells.

608 A sequential triple-drug regimen combining TAS102-talazoparib and WEE1i showed robust
609 anti-tumor effects in preclinical animal models (**Fig. 7**). Tumor growth was reduced by 63% in
610 the CRC HT29 tumor model and ~80% in the PDAC PDX-14312 model ($p53^{R175H}$) (**Fig.7**).
611 Further, the triple-drug treatment was also highly effective in reducing tumor growth in CRC
612 PDX model (~55%). No major toxic side effects were observed during assessment of mouse
613 weight, bone marrow, and peripheral blood.

614 In summary, this study presents a sequential triple-drug strategy combining TAS102-PARPi
615 treatment with delayed application of a G2-kinase inhibitor (WEE1i), which together work as an
616 *inducer-amplifier-terminator trio* (**Fig.7m**). The TAS102-talazoparib regimen was well tolerated
617 in patients with refractory CRC and showed promising median progression-free survival (mPFS)
618 of 5.7 months (NCT04511039) [37]. This study showed that a sequential G2-kinase blockade with
619 WEE1i strongly enhances efficacy of TAS102-talazoparib in p53mut cancers. This sequential
620 triple-drug strategy is a promising approach for management of patients with p53mut cancers.
621

622 **Limitations of the Study**

623 This study demonstrated the increased efficacy of TAS102-PARPi treatment in combination with
624 a subsequent administration of WEE1i in p53mut CRC and PDAC models. Although, prior work
625 has shown that TAS102-PARPi treatment can block breast cancer metastases [17], the current study

626 did not directly assess the effect of the combinatorial drug treatment on metastatic burden (e.g.,
627 liver) in PDAC and CRC *in vivo* models. This question is the subject of future research.
628

629 **AUTHOR CONTRIBUTIONS**

630 A.V.B. conceived the idea; A.V.B., R.M.S., J.Z., and M.M.A. designed the experiments; J.Z.,
631 M.M.A., A.V.B, M.N.N and B.G. performed the experiments and analyzed the data; A.V.B. and
632 C.F. analyzed and interpreted the data; T.M. and R.M.S. helped in the interpretation of the data;
633 B.G., B.F., S.C. helped with PDX generation; A.V.B., C.F., T.M., J.Z., M.M.A., R.M.S. and R.I.
634 contributed to preparing and writing the paper.
635

636 **ACKNOWLEDGEMENT**

637 We gratefully acknowledge the generous help from Flow and Image Cytometry Facility, the
638 Pathology Resource Network, Preclinical Imaging Services, Experimental Tumor Model Shared
639 Resource, and Laboratory Animal Resource (LAR), Ninfa L. Straubinger for technical assistance
640 with the PDAC models. We thank Drs. Bert Vogelstein and Alessandro Carugo for their
641 generous gifts of cell lines, Drs. Dean Tang and David Goodrich for discussion of the
642 manuscript. This work supported by NIH R21CA259719 and DoD BC220542 (to AVB), NIH
643 R37CA282430 (to CF and AVB), Roswell Park Alliance Foundation (to AVB and CF), NIH
644 R01CA198096 to R.M.S., NIH grant AI164081 (to TM), in part by NIH R25CA181003, the
645 Deanship of Scientific Research at Northern Border University, Arar, KSA the project number
646 "NBU-SAFIR-2024 to (MMA), and the Roswell Park Comprehensive Cancer Center Support
647 Grant, P30CA016056. Research reported in this publication was supported by the National
648 Institutes of Health Office of Research Infrastructure Programs under award number
649 S10OD024973 [49]. The content is solely the responsibility of the authors and does not necessarily
650 represent the official views of the National Institutes of Health. Computational support was
651 provided by the Center for Computational Research at the University at Buffalo [50].

652 **ETHICS STATEMENT**

653 The study protocol was approved by the Institute Animal Care and Use Committee (IACUC).
654 The facility was certified by the American Association for Accreditation of Laboratory Animal
655 Care (AAALAC) and in accordance with the current regulations and standards of the US
656 Department of Agriculture and the US Department of Health and Human Services.
657

658 **MATERIALS AVAILABILITY**

659 Patient-derived xenograft colorectal cancer models are available from the lead contact (A.B.)
660 under a Material Transfer Agreement.
661

662 **LEAD CONTACT**

663 Further information and requests for resources and reagents should be directed to and will be
664 fulfilled by the lead contact, prof. Andrei Bakin (Andrei.Bakin@roswellpark.org)

665

666 **FIGURE LEGENDS**

667 **Figure 1. The combination of TAS102 and talazoparib induces DNA damage response and**
668 **the G2 checkpoint.** (**a-b**) Cell-cycle analysis of HCT116 p53WT and p53KO, and DLD1
669 ($p53^{S241F}$) cell lines treated with vehicle control (C), 100nM talazoparib (Tal), 500 nM TAS102
670 (TAS) or their combination (TAS+Tal) for 24 hours. Cells were stained with Hoechst for DNA
671 content and analyzed by flow cytometry. (**b**) Quantification of cell cycle data. Comparisons were
672 made using two-way ANOVA (∗p < 0.05, ∗∗p < 0.01, ∗∗∗p < 0.001, ∗∗∗∗p < 0.0001).
673 Experiments were repeated at least two times. (**c-d**) Immunoblots of whole-cell extracts from cell
674 lines treated with vehicle control (C), 100 nM talazoparib (T), 500 nM TAS102 (TAS), their
675 combination (TT), or 50 nM nocodazole (Nc) for 24 hours. (**e-f**) Quantification of phospho-
676 CDK1 and phospho-H3 levels in CRC PDX-02-07-RP ($p53^{H179R}$) tissues (**e**), and PDX-01-03-RP
677 (p53WT) tissues (**f**). PDX tumor bearing mice were treated by oral gavage with vehicle-control,
678 talazoparib, TAS102, or TAS102-talazoparib. Comparisons were done using one-way ANOVA
679 (*p < 0.05, **p < 0.01, ***p < 0.001, and ****p < 0.0001). (**g**) Working model.

680

681 **Figure 2. Transcriptomic changes in p53WT and p53KO cells following TAS102 and**
682 **talazoparib treatment.** Volcano plots show differential gene expression between control and
683 treatment groups (talazoparib, TAS102, and combination) for both HCT116 p53WT (**a-c**) and
684 p53KO (**d-f**) cell lines. Red data points represent genes that meet both the adjusted p-value <0.05
685 and a pre-defined log2 fold change (FC) threshold. Blue data points indicate genes that only meet
686 the log2 FC threshold, gray dots show non-significant genes. (**g-h**) Venn diagrams show the
687 overlap of differentially expressed genes among the treatment groups in HCT116 p53WT (**g**) and
688 p53KO (**h**) cells. (**i**) Heatmaps show the expression profiles of select genes across the control and
689 treatment groups in HCT116 p53WT (left) and p53KO (right) cells. Gene lists are curated from
690 KEGG and Cyclebase_3.0 databases.

691

692 **Figure 3. G2 checkpoint kinase inhibitors enhance the cytotoxic effects of TAS102 and**
693 **talazoparib treatment.** (**a-d**) Dose-response curves for a panel of colorectal cancer cell lines
694 treated with increasing concentrations of TAS102 in the presence of 100 nM talazoparib. Cells
695 were co-treated for 72 hours with varying concentrations of the ATR inhibitor AZD6738
696 (ATRi; 50nM, 100nM, 250nM, and 500nM). (**e-i**) Cells were treated as described above with the
697 CHK1 inhibitor, AZD7762 (CHK1i; 50, 100, 250, and 500 nM). (**j-m**) Cells were treated as
698 described above with the WEE1 inhibitor, MK-1775 (WEE1i; 50, 100, 250, and 500 nM). All
699 data were normalized to untreated control. The half-maximal inhibitory concentration (IC50)
700 values were determined using three-parameter nonlinear regression. All experiments were
701 performed with at least two biological replicates and six technical replicates. (**n-o**) Cytotoxicity
702 parameters in p53WT and mutant cell lines. Combination Index (CI) values were calculated for
703 combinations with ATRi (**n**) and WEE1i (**o**) across several concentrations.

704

705 **Figure 4. Combination treatment with TAS102 and talazoparib induces a prolonged G2**
706 **arrest in p53-mutant cancer cells.** (**a-c**) Cell cycle analysis was performed on cell lines treated
707 with vehicle control (C), 500nM TAS102 and 100nM talazoparib for 24 hours (**T0**) followed by
708 incubation in drug-free medium. All experiments were done in at least two independent
709 biological replicates. (**d-g**) Immunoblotting on whole-cell extracts from HCT116-p53WT,
710 HCT116-p53KO, HCT116-p53$^{R248W/-}$ and HT29 cell lines treated as described above (**a-c**). The
711 experiments were repeated in at least two independent biological replicates and two technical
712 replicates. Blots were probed with antibodies to phopsho-CHK1, p53, cyclin D1, phospho-
713 CDK1, p21, phospho-H2AX (γH2AX), phospho-histone H3, and GAPDH as a loading control.
714
715 **Figure 5. The dynamics of DNA damage repair in response to combined TAS102 and**
716 **talazoparib treatment.** (**a**) Immunofluorescence microscopy images of p53WT cells stained for
717 γH2AX (green), a DNA damage marker, and RAD51 (red), a homologous recombination
718 component, along with Hoechst 33342 (blue; nucleus). Cells were treated with vehicle-control
719 (CTR) or 500nM TAS102 plus 100nM talazoparib (**T0**) for 24 hours, followed by drug
720 withdrawal and the cells were allowed to recover. All images were taken using 100x lens; scale
721 bar 10μm. (**b, h**) Enlarged images of regions highlighted in the main panels show the co-
722 localization of γH2AX and RAD51 foci at T0 in MCF10A cells and at 24 hours in DLD1 cells.
723 Arrows indicate the positions of these foci. (**c**) Enlarged images of Hoechst-stained cells at CTR,
724 T0, and 72hours. (**d-e, j-k, m-n**) Quantitative analysis of corrected total cellular fluorescence
725 (CTCF) for γH2AX (**d, j, m**) and RAD51 (**e, k, n**) was performed on a minimum 40 cells per
726 treatment group. The graphs show representative median scattered dot plots. Comparisons were
727 made using the two-way ANOVA (****, P<0.001). (**f, l, o**) The nuclear area was measured from
728 Hoechst-stained cells, with at least 40 cells/group. All experiments were done at least two times.
729
730 **Figure 6. Sequential application of WEE1 inhibitor enhances the cytotoxicity of TAS102-**
731 **talazoparib treatment in p53-deficient cancer cells.** (**a-e**) Cytotoxicity curves for p53 wild-
732 type (MCF10A and HCT116), and p53-deficient (HCT116-p53KO, HCT116-p53$^{R248W/-}$, HT29)
733 cells. Cells were treated with increasing concentrations of TAS102 plus 100nM talazoparib for
734 24 hours. After a 24-hour drug washout, cells were incubated with 50, 100, 250, or 500 nM of
735 the WEE1 inhibitor (WEE1i) for an additional 72 hours. (**f**) Combination index (CI) analysis for
736 the tested WEE1i concentrations. Data are presented as mean ± SEM from at least two
737 independent biological replicates, each with six technical replicates. (**g**) Flow cytometry analysis
738 of cells treated with vehicle control or a sequential regimen of 500 nM TAS102 plus 100 nM
739 talazoparib, followed by 250 nM WEE1i. Cells were stained with propidum iodide and annexin-
740 V. (**h-k**) Quantification of Annexin V and propidium iodide (PI) double-positive cells from two
741 biological replicates. Statistical significance was determined using one-way ANOVA (*$p < 0.05$,
742 **$p < 0.01$, ***$p < 0.001$, and ****$p < 0.0001$).
743
744 **Figure 7. A sequential application of WEE1 inhibitor enhances the efficacy of TAS102-**
745 **talazoparib treatment in p53 mutant cancer models.** (**a-d**) SCID mice (10mice/group) were
746 subcutaneously implanted with colon cancer HT29 cells. At tumor size of 100mm^3, mice were
747 randomized into four treatment groups: vehicle control, WEE1 inhibitor (WEE1i, MK1775, 60
748 mg/kg), a combination of TAS102 (50 mg/kg) and talazoparib (0.15 mg/kg), and a sequential
749 regimen consisting of one week of TAS102/talazoparib followed by one week of the WEE1

750 inhibitor. All treatments were administered *via* oral gavage on a schedule of five days ON and
751 two days OFF. Tumor growth was measured twice weekly, and statistical significance was
752 determined using a two-way ANOVA (*$p < 0.05$). (**b**) Tumor growth inhibition (TGI) was
753 calculated as TGI = 100% x [Vehicle − Treatment) / Vehicle]. Comparisons were made using a
754 one-way ANOVA (**, P<0.01, ***, P<0.001, ****, P<0.001). (**c**) Survival was evaluated using
755 Kaplan-Meier estimator based on time-to-arrive at 750 mm^3 of tumor size. The comparison was
756 made using the log-rank test. (**d**) Mouse body weights were measured twice per week over the
757 course of study. (**e-h**) Patient-derived tumor xenografts (PDXs) from a patient with PDAC
758 (PDAC-14312-4p) were subcutaneously implanted into SCID mice (10 mice/group). At 100
759 mm^3, mice were randomized and treated as described above for HT29 xenografts. (**f**) Tumor
760 growth inhibition in the PDX model was calculated as described in (**b**). Comparisons were made
761 using a one-way ANOVA (**, P<0.01, ***, P<0.001, ****, P<0.001). (**g**) Survival was evaluated
762 using Kaplan-Meier estimator based on time to arrive at 750 mm3 of tumor size. Group
763 comparisons were performed with the log-rank test. (**h**) Mouse body weights were measured
764 twice weekly over the course of study. (**i-l**) Patient-derived tumor xenografts (PDXs) from a
765 colorectal cancer patient (PDX-3B1-29-RP-3p) were subcutaneously implanted into SCID mice
766 (10 mice/group). Experiments and the analysis were done essentially as described for (**e-h**). (**m**)
767 A model of the triple-drug drug strategy acting as an *inducer-amplifier-terminator* trio in p53
768 mutant cancers.
769

770 **REFERENCES**

771 1. Siegel RL, Giaquinto AN, Jemal A. Cancer statistics, 2024. CA Cancer J Clin.
772 2024;74(1):12-49.
773 2. Ladabaum U, Dominitz JA, Kahi C, Schoen RE. Strategies for Colorectal Cancer Screening.
774 Gastroenterology. 2020;158(2):418-32.
775 3. Patel SG, Karlitz JJ, Yen T, Lieu CH, Boland CR. The rising tide of early-onset colorectal
776 cancer: a comprehensive review of epidemiology, clinical features, biology, risk factors,
777 prevention, and early detection. Lancet Gastroenterol Hepatol. 2022;7(3):262-74.
778 4. Siegel RL, Wagle NS, Cercek A, Smith RA, Jemal A. Colorectal cancer statistics, 2023. CA
779 Cancer J Clin. 2023;73(3):233-54.
780 5. Biller LH, Schrag D. Diagnosis and Treatment of Metastatic Colorectal Cancer: A Review.
781 Jama. 2021;325(7):669-85.
782 6. Wolfgang CL, Herman JM, Laheru DA, Klein AP, Erdek MA, Fishman EK, et al. Recent
783 progress in pancreatic cancer. CA Cancer J Clin. 2013;63(5):318-48.
784 7. Neoptolemos JP, Kleeff J, Michl P, Costello E, Greenhalf W, Palmer DH. Therapeutic
785 developments in pancreatic cancer: current and future perspectives. Nature reviews
786 Gastroenterology & hepatology. 2018;15(6):333-48.
787 8. Nakayama M, Oshima M. Mutant p53 in colon cancer. J Mol Cell Biol. 2019;11(4):267-76.
788 9. Muller PAJ, Vousden KH. Mutant p53 in cancer: new functions and therapeutic
789 opportunities. Cancer Cell. 2014;25(3):304-17.
790 10. Sabapathy K, Lane DP. Therapeutic targeting of p53: all mutants are equal, but some mutants
791 are more equal than others. Nature reviews Clinical oncology. 2018;15(1):13-30.
792 11. Wang H, Guo M, Wei H, Chen Y. Targeting p53 pathways: mechanisms, structures, and
793 advances in therapy. Signal Transduct Target Ther. 2023;8(1):92.
794 12. Reinhardt HC, Aslanian AS, Lees JA, Yaffe MB. p53-deficient cells rely on ATM- and
795 ATR-mediated checkpoint signaling through the p38MAPK/MK2 pathway for survival after
796 DNA damage. Cancer Cell. 2007;11(2):175-89.
797 13. Mendez E, Rodriguez CP, Kao MC, Raju S, Diab A, Harbison RA, et al. A Phase I Clinical
798 Trial of AZD1775 in Combination with Neoadjuvant Weekly Docetaxel and Cisplatin before
799 Definitive Therapy in Head and Neck Squamous Cell Carcinoma. Clin Cancer Res.
800 2018;24(12):2740-8.
801 14. Leijen S, Beijnen JH, Schellens JH. Abrogation of the G2 checkpoint by inhibition of Wee-1
802 kinase results in sensitization of p53-deficient tumor cells to DNA-damaging agents. Current
803 clinical pharmacology. 2010;5(3):186-91.
804 15. Durinikova E, Reilly NM, Buzo K, Mariella E, Chilà R, Lorenzato A, et al. Targeting the
805 DNA Damage Response Pathways and Replication Stress in Colorectal Cancer. Clinical cancer
806 research : an official journal of the American Association for Cancer Research.
807 2022;28(17):3874-89.
808 16. Lheureux S, Cristea MC, Bruce JP, Garg S, Cabanero M, Mantia-Smaldone G, et al.
809 Adavosertib plus gemcitabine for platinum-resistant or platinum-refractory recurrent ovarian
810 cancer: a double-blind, randomised, placebo-controlled, phase 2 trial. Lancet.
811 2021;397(10271):281-92.
812 17. Zonneville J, Wang M, Alruwaili MM, Smith B, Melnick M, Eng KH, et al. Selective
813 therapeutic strategy for p53-deficient cancer by targeting dysregulation in DNA repair.
814 Communications biology. 2021;4(1):862.

815 18. Alruwaili MM, Zonneville J, Naranjo MN, Serio H, Melendy T, Straubinger RM, et al. A
816 synergistic two-drug therapy specifically targets a DNA repair dysregulation that occurs in p53-
817 deficient colorectal and pancreatic cancers. Cell Rep Med. 2024;5(3):101434.
818 19. Fountzilas C, Witkiewicz A, Chatley S, Fitzpatrick V, Zonneville J, Alruwaili M, et al.
819 YIA24-003: A Phase I Study of TAS102 Plus Talazoparib in Advanced Colorectal (CRC) and
820 Esophagogastric (EGC) Adenocarcinomas. Journal of the National Comprehensive Cancer
821 Network. 2024;22(2.5):YIA24-003.
822 20. Voit R, Seiler J, Grummt I. Cooperative Action of Cdk1/cyclin B and SIRT1 Is Required for
823 Mitotic Repression of rRNA Synthesis. PLoS genetics. 2015;11(5):e1005246.
824 21. Smith J, Tho LM, Xu N, Gillespie DA. The ATM-Chk2 and ATR-Chk1 pathways in DNA
825 damage signaling and cancer. Advances in cancer research. 2010;108:73-112.
826 22. Castedo M, Perfettini JL, Roumier T, Andreau K, Medema R, Kroemer G. Cell death by
827 mitotic catastrophe: a molecular definition. Oncogene. 2004;23(16):2825-37.
828 23. Xie G, Habbersett RC, Jia Y, Peterson SR, Lehnert BE, Bradbury EM, et al. Requirements
829 for p53 and the ATM gene product in the regulation of G1/S and S phase checkpoints.
830 Oncogene. 1998;16(6):721-36.
831 24. Toledo LI, Murga M, Fernandez-Capetillo O. Targeting ATR and Chk1 kinases for cancer
832 treatment: a new model for new (and old) drugs. Mol Oncol. 2011;5(4):368-73.
833 25. Lobrich M, Jeggo PA. The impact of a negligent G2/M checkpoint on genomic instability
834 and cancer induction. Nat Rev Cancer. 2007;7(11):861-9.
835 26. Peng C-Y, Graves PR, Thoma RS, Wu Z, Shaw AS, Piwnica-Worms H. Mitotic and
836 G₂ Checkpoint Control: Regulation of 14-3-3 Protein Binding by Phosphorylation
837 of Cdc25C on Serine-216. Science. 1997;277(5331):1501-5.
838 27. Sanchez Y, Wong C, Thoma RS, Richman R, Wu Z, Piwnica-Worms H, et al. Conservation
839 of the Chk1 Checkpoint Pathway in Mammals: Linkage of DNA Damage to Cdk Regulation
840 Through Cdc25. Science. 1997;277(5331):1497-501.
841 28. Solomon MJ, Lee T, Kirschner MW. Role of phosphorylation in p34cdc2 activation:
842 identification of an activating kinase. Mol Biol Cell. 1992;3(1):13-27.
843 29. Krek W, Nigg EA. Mutations of p34cdc2 phosphorylation sites induce premature mitotic
844 events in HeLa cells: evidence for a double block to p34cdc2 kinase activation in vertebrates.
845 EMBO J. 1991;10(11):3331-41.
846 30. Lee TH, Kirschner MW. An inhibitor of p34cdc2/cyclin B that regulates the G2/M transition
847 in Xenopus extracts. Proc Natl Acad Sci U S A. 1996;93(1):352-6.
848 31. Sausville E, Lorusso P, Carducci M, Carter J, Quinn MF, Malburg L, et al. Phase I dose-
849 escalation study of AZD7762, a checkpoint kinase inhibitor, in combination with gemcitabine in
850 US patients with advanced solid tumors. Cancer Chemother Pharmacol. 2014;73(3):539-49.
851 32. Seto T, Esaki T, Hirai F, Arita S, Nosaki K, Makiyama A, et al. Phase I, dose-escalation
852 study of AZD7762 alone and in combination with gemcitabine in Japanese patients with
853 advanced solid tumours. Cancer Chemother Pharmacol. 2013;72(3):619-27.
854 33. Foote KM, Nissink JWM, McGuire T, Turner P, Guichard S, Yates JWT, et al. Discovery
855 and Characterization of AZD6738, a Potent Inhibitor of Ataxia Telangiectasia Mutated and Rad3
856 Related (ATR) Kinase with Application as an Anticancer Agent. J Med Chem.
857 2018;61(22):9889-907.
858 34. Leijen S, van Geel RM, Pavlick AC, Tibes R, Rosen L, Razak AR, et al. Phase I Study
859 Evaluating WEE1 Inhibitor AZD1775 As Monotherapy and in Combination With Gemcitabine,

860 Cisplatin, or Carboplatin in Patients With Advanced Solid Tumors. J Clin Oncol.
861 2016;34(36):4371-80.
862 35. Chou TC, Talalay P. Quantitative analysis of dose-effect relationships: the combined effects
863 of multiple drugs or enzyme inhibitors. Adv Enzyme Regul. 1984;22:27-55.
864 36. Foucquier J, Guedj M. Analysis of drug combinations: current methodological landscape.
865 Pharmacol Res Perspect. 2015;3(3):e00149.
866 37. Fountzilas C, Witkiewicz A, Chatley S, Fitzpatrick V, Zonneville J, Alruwaili M, et al. A
867 Phase I Study of TAS102 Plus Talazoparib in Advanced Colorectal (CRC) and Esophagogastric
868 (EGC) Adenocarcinomas. Journal of the National Comprehensive Cancer Network.
869 2024;22(2.5):YIA24-003.
870 38. Shirole NH, Pal D, Kastenhuber ER, Senturk S, Boroda J, Pisterzi P, et al. TP53 exon-6
871 truncating mutations produce separation of function isoforms with pro-tumorigenic functions.
872 eLife. 2016;5:e17929.
873 39. Barr PJ, Nolan PA, Santi DV, Robins MJ. Inhibition of thymidylate synthetase by 5-alkynyl-
874 2'-deoxyuridylates. Journal of medicinal chemistry. 1981;24(12):1385-8.
875 40. Pettersen HS, Visnes T, Vagbo CB, Svaasand EK, Doseth B, Slupphaug G, et al. UNG-
876 initiated base excision repair is the major repair route for 5-fluorouracil in DNA, but 5-
877 fluorouracil cytotoxicity depends mainly on RNA incorporation. Nucleic Acids Res.
878 2011;39(19):8430-44.
879 41. Murai J, Huang SY, Das BB, Renaud A, Zhang Y, Doroshow JH, et al. Trapping of PARP1
880 and PARP2 by Clinical PARP Inhibitors. Cancer Res. 2012;72(21):5588-99.
881 42. Shiloh Y, Ziv Y. The ATM protein kinase: regulating the cellular response to genotoxic
882 stress, and more. Nat Rev Mol Cell Biol. 2013;14(4):197-210.
883 43. Lavin MF. ATM and the Mre11 complex combine to recognize and signal DNA double-
884 strand breaks. Oncogene. 2007;26(56):7749-58.
885 44. Zhang X, Li J, Sejas DP, Pang Q. The ATM/p53/p21 pathway influences cell fate decision
886 between apoptosis and senescence in reoxygenated hematopoietic progenitor cells. J Biol Chem.
887 2005;280(20):19635-40.
888 45. Saldivar JC, Hamperl S, Bocek MJ, Chung M, Bass TE, Cisneros-Soberanis F, et al. An
889 intrinsic S/G(2) checkpoint enforced by ATR. Science. 2018;361(6404):806-10.
890 46. Foo TK, Vincelli G, Huselid E, Her J, Zheng H, Simhadri S, et al. ATR/ATM-Mediated
891 Phosphorylation of BRCA1 T1394 Promotes Homologous Recombinational Repair and G(2)-M
892 Checkpoint Maintenance. Cancer Res. 2021;81(18):4676-84.
893 47. Rogakou EP, Pilch DR, Orr AH, Ivanova VS, Bonner WM. DNA double-stranded breaks
894 induce histone H2AX phosphorylation on serine 139. J Biol Chem. 1998;273(10):5858-68.
895 48. Britton S, Chanut P, Delteil C, Barboule N, Frit P, Calsou P. ATM antagonizes NHEJ
896 proteins assembly and DNA-ends synapsis at single-ended DNA double strand breaks. Nucleic
897 Acids Res. 2020;48(17):9710-23.
898 49. Furlani T, Matott L. Acquisition of High-Performance Data and Computing Infrastructure to
899 Advance Biomedical Research2019.
900 50. UBCCR. Center for Computational Research, University at Buffalo. 2021. CCR Facility
901 Description.
902

903

904 **KEY RESOURCES TABLE**

REAGENT or RESOURCE	SOURCE	IDENTIFIER
Antibodies		
anti-p53 (Mouse Monoclonal antibody, Clone do-1)	Santa Cruz Biotechnology	Cat# sc-126; RRID:AB_628082
anti-p21 (CDKN1A), F-5 mouse monoclonal	Santa Cruz Biotechnology	Cat# sc-6246; RRID:AB_628073
anti-phospho-Ser15 p53 (rabbit, polyclonal)	Cell Signaling Technology	Cat# 9284; RRID:AB_331464
anti-PARP1 (mouse monoclonal antibody, Clone 5a5)	Santa Cruz Biotechnology	Cat# sc-56197; RRID:AB_630080
anti-phospho-Ser139 H2AX (γH2AX; rabbit polyclonal)	Abcam	Cat# ab-11174; RRID:AB_297813
anti-Thymidylate Synthase (TS106)	Millipore	Cat# MAB4130, RRID:AB_2210729
anti-phospho-Tyr15-CdC2	Santa Cruz	Cat# sc-136014, RRID:AB_2016914
anti-phospho-Chk1 (Ser325)	Cell signaling	Cat# 2348, RRID:AB_331212
anti-phospho HH3 (Ser10)	Cell signaling	Cat# 31261, RRID:AB_3076725
anti-Cyclin A2	Invitrogen	Cat# MA1-180, RRID:AB_2633305
anti-bromodeoxyuridine, anti-BrdU	Dako	Cat# M0744, RRID:AB_10013660
anti-cleaved Caspase-3 (Asp175)	Cell signaling	Cat# 9661, RRID:AB_2341188
Rabbit anti-gamma-H2AX (phospho-Ser139) Antibody	Bethyl	Cat# A300-081A, RRID:AB_203288
anti-Human Ki67/MKI67 Antibody	R&D Systems	Cat#: IC7617S, RRID:AB_2889352
anti-Rad51 antibody	Abcam	Cat# ab133534, RRID:AB_2722613
anti-phospho-Ser139 H2AX (γH2AX; mouse mAb, JBW301)	Millipore	Cat# 05-636; RRID:AB_309864
anti-BrdU antibody (3D4), FITC conjugate	Biolegend	Cat#364104; RRID:AB_2564481
Goat Anti-Rabbit IgG (H L)-HRP Conjugate antibody	Bio-Rad	Cat# 170-6515; RRID:AB_11125142
Goat Anti-Mouse IgG (H L)-HRP Conjugate antibody	Bio-Rad	Cat# 170-6516; RRID:AB_11125547
Biological samples: Patient Derived Xenografts (PDXs)		
PDAC PDX-14312-4p	Dr. Robert Straubinger (University at Buffalo)	SUNY at Buffalo
CRC PDX-3B1-29-RP-3p	Dr. Andrei Bakin (Roswell Park)	PDX-3B1-29-RP

Chemicals, peptides, and recombinant proteins		
Talazoparib (Synonyms: BMN-673)	Adooq	Cat# A15533
TAS102 (trifluorthymidine (trifluridine)/tipiracil HCl mix)	Adooq	Cat# A11243
5-ethynyl-2'-deoxyuridine (EdUrd)	Lumiprobe	Cat# 20540
Cy3-azide	Lumiprobe	Cat#B1030
CellTrace Violet Dye	Invitrogen	Cat#C34557
AFDye 488 Azide	Click Chemistry Tools, Scottsdale, AZ	Cat#1275-1
THPTA (tris-hydroxypropyltriazolylmethylamine)	Click Chemistry Tools, Scottsdale, AZ	Cat#1010-500
RNase A (10 mg/mL)	Thermo Fisher Scientific	Cat#EN0531
D-luciferin	Gold Biotechnology, St Louis	LUCK-1G
Copper sulfate, Cu(II)SO4	Sigma-Aldrich	Cat# 61230
Hydroxyurea	Sigma-Aldrich	Cat#55291
(2-Hydroxypropyl)-β-cyclodextrin (HPCD; Cavasol)	Sigma-Aldrich	Cat#778907
Bovine serum albumin (BSA)	Sigma-Aldrich	Cat#A2153
Dimethyl sulfoxide (DMSO)	Sigma-Aldrich	Cat#D8418
Boric acid	Sigma-Aldrich	Cat#B6768
Propidium iodide	Sigma-Aldrich	Cat#P4170
Hoechst 33342	Sigma-Aldrich	Cat#B2261
Methylene Blue hydrate	Sigma-Aldrich	Cat#M9140-100G
Paraformaldehyde	Sigma-Aldrich	Cat#158127
Dialyzed FBS (fetal bovine serum)	Gibco	Cat#A33820
ECL Western Blotting Substrate, Pierce	Thermo Fisher Scientific	Cat# 32106
SuperSignal™ West Atto Ultimate Sensitivity Substrate	Thermo Fisher Scientific	Cat#A38555
SDS (Sodium Dodecyl Sulfate)	Bio-Rad	Cat#1610301
DC™ Protein Assay Kit I	Bio-Rad	Cat#5000111
Tween 20, 100% Nonionic Detergent	Bio-Rad	Cat#1706531
Matrigel Matrix GFR	VWR International	Cat# 47743-720
Critical commercial assays		
Caspase-Glo® 3/7 Assay System	Promega	Cat#G8090
Deposited data		
Gene Expression and Mutation Counts	Pan-CANCER-TCGA	Cbioportal.org
Experimental models: Cell lines		
HCT-116 (p53-WT)	Dr. Bert Vogelstein (Johns Hopkins)	RRID:CVCL_0291
HCT-116-p53-KO; HCT-116 TP53(-/-); HCT116-p53-null	Dr. Bert Vogelstein (Johns Hopkins)	RRID:CVCL_HD97

HCT-116-p53-R248W/-	Dr. Bert Vogelstein (Johns Hopkins)	RRID:CVCL_RJ68
RKO	Dr. Alessandro Carugo (IRBM European School of Molecular Medicine, Lazio, Italia)	RRID:CVCL_0504
RKO-p53(-/-); RKO-p53KO; RKO-p53-null	Dr. Alessandro Carugo (IRBM ESMM, Lazio, Italia)	
HT29; HT-29	ATCC	RRID:CVCL_0320
MIAPACA2; MiaPaCa-2	ATCC	RRID:CVCL_0428
MCF10A	ATCC	RRID:CVCL_0598
MDA-MB-231	ATCC	RRID:CVCL_0062
HPNE; hTERT-Human Pancreatic Nestin-Expressing cells	ATCC	RRID:CVCL_C466
DLD1	ATCC	RRID:CVCL_0248
PANC-1	ATCC	RRID:CVCL_0480
Experimental models: Organisms/strains		
Mouse: SCID/CB17, Balb/c background	Roswell Park Colony	
Mouse: NOD.Cg-Prkdcscid Il2rgtm1Wjl/SzJ (NSG) mice, Balb/c background	Jackson Laboratory	
Software and algorithms		
GraphPad PRISM 10.1.2	GraphPad Software	https://www.graphpad.com/
R/RStudio v4.0.4	The R Foundation	https://www.r-project.org/
FCS Express 7 (Version 7.04.0016)	De Novo software	FCS Express Flow Cytometry Software - De Novo Software
Image J	NIH	https://imagej.net/software/imagej/
HeskaView Integrated Software (version 2.5.2)	Heska	Element HT5 - Heska
Aperio ImageScope (version 12.4.0.5043)	Leica Biosystems	
MetaVue imaging software (Version 7.7.3)	Molecular Devices	
FACSDiva (Version 6.1.3)	Beckman Coulter	
Other		
Nikon TE2000-E inverted microscope	Nikon, USA	
CoolSNAP HQ (CCD camera)	Photometrics, USA	
LSRFortessa Cytometer	BD Biosciences, USA	
VERITAS microplate luminometer	Promega, USA	
Nanodrop	Thermo Fisher, USA	

905

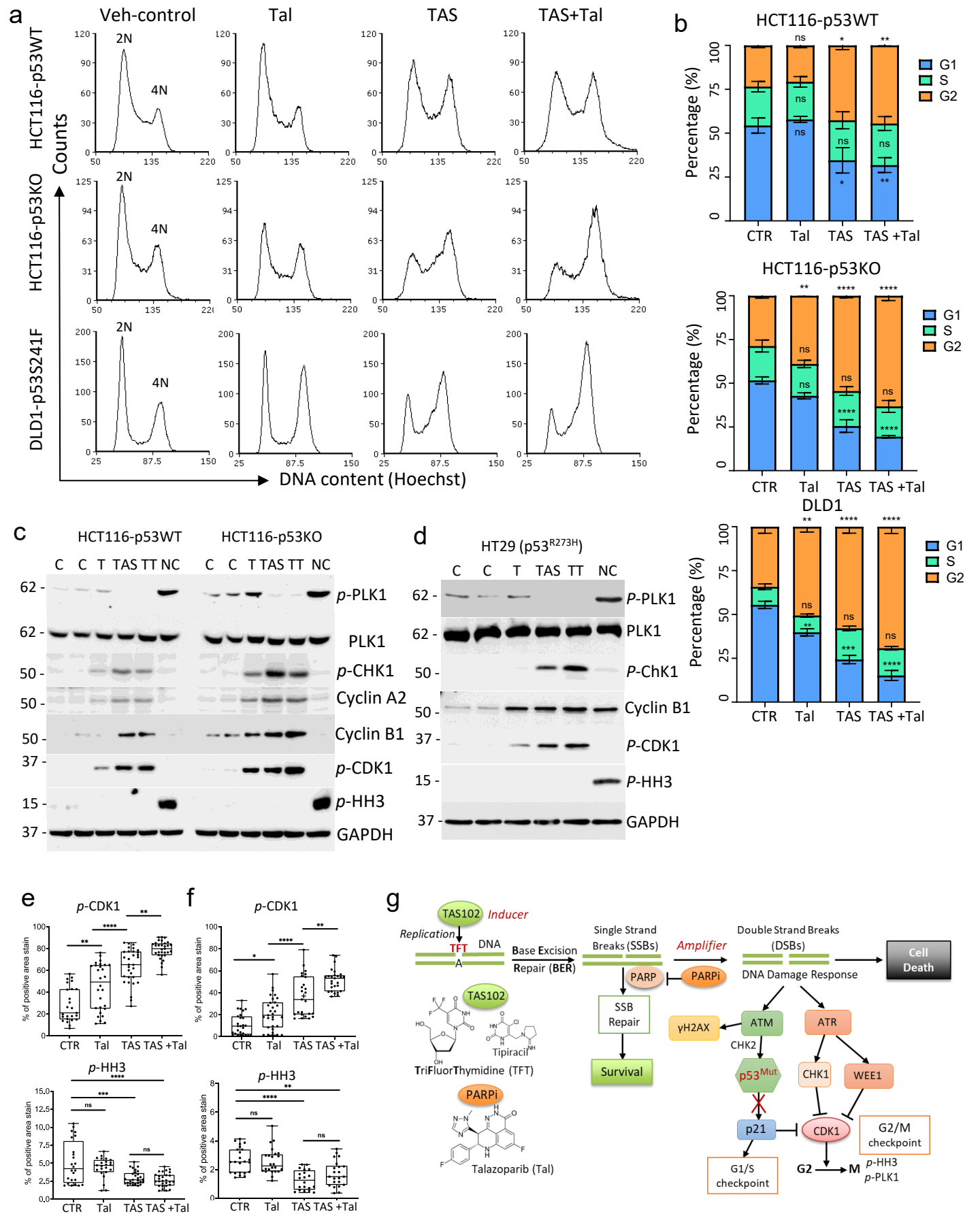
a
Veh-control
Tal
TAS
TAS+Tal
HCT116-p53WT
HCT116-p53KO
DLD1-p53S241F
Counts
2N
4N
DNA content (Hoechst)
b
HCT116-p53WT
HCT116-p53KO
DLD1
Percentage (%)
G1
S
G2
CTR
Tal
TAS
TAS +Tal
c
HCT116-p53WT
HCT116-p53KO
C C T TAS TT NC
p-PLK1
PLK1
p-CHK1
Cyclin A2
Cyclin B1
p-CDK1
p-HH3
GAPDH
d
HT29 (p53R273H)
C C T TAS TT NC
P-PLK1
PLK1
P-ChK1
Cyclin B1
P-CDK1
P-HH3
GAPDH
e
p-CDK1
p-HH3
% of positive area stain
CTR
Tal
TAS
TAS +Tal
f
p-CDK1
p-HH3
% of positive area stain
CTR
Tal
TAS
TAS +Tal
g
TAS102
Inducer
Replication
TFT
DNA
A
Base Excision Repair (BER)
Single Strand Breaks (SSBs)
Amplifier
Double Strand Breaks (DSBs)
Cell Death
PARP
PARPi
DNA Damage Response
SSB Repair
Survival
γH2AX
ATM
ATR
CHK2
p53Mut
CHK1
WEE1
p21
CDK1
G2/M checkpoint
G1/S checkpoint
G2
M
p-HH3
p-PLK1
TAS102
Tipiracil
TriFluorThymidine (TFT)
PARPi
Talazoparib (Tal)

Fig. 2

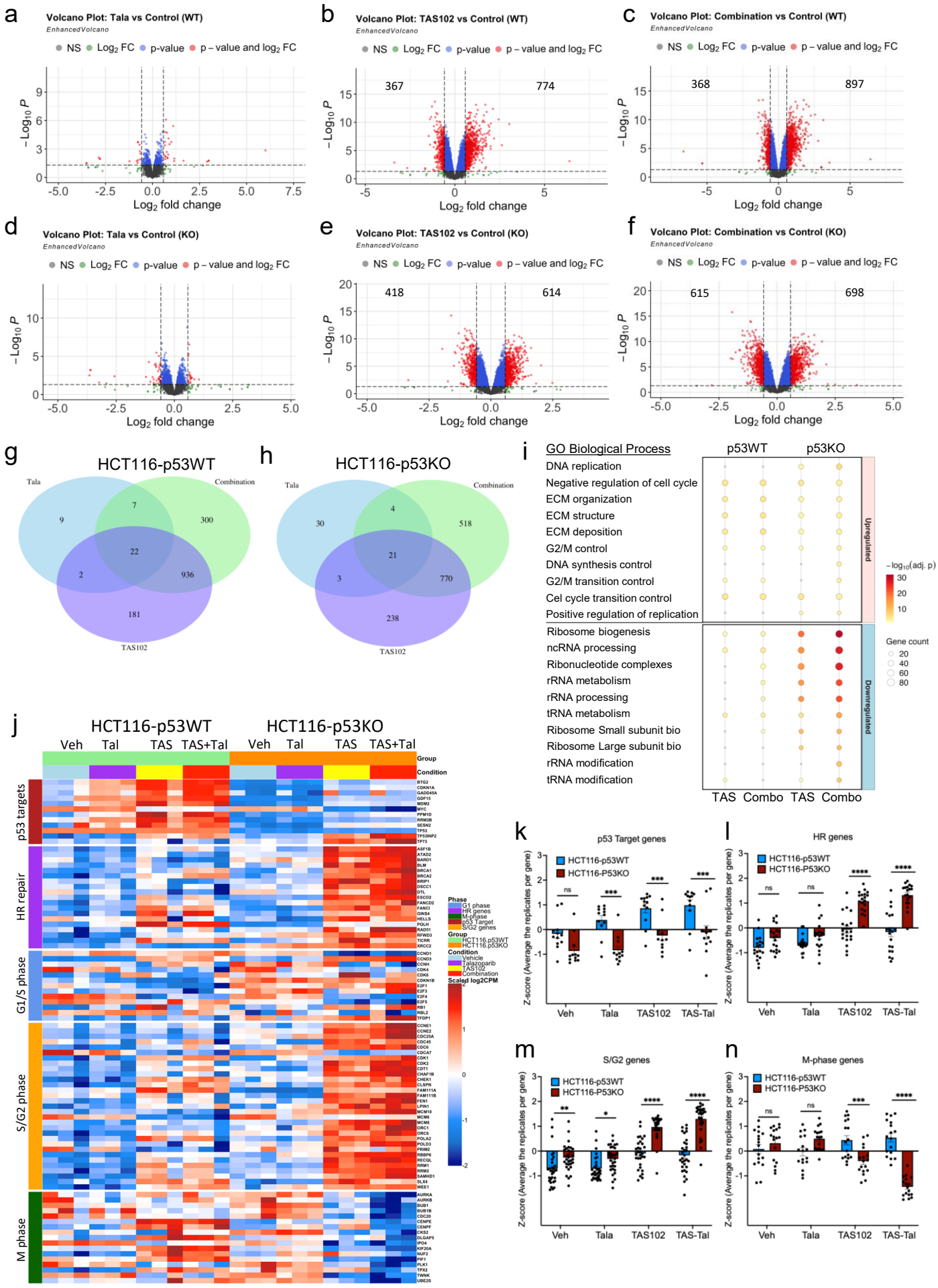
a
Volcano Plot: Tala vs Control (WT)
b
Volcano Plot: TAS102 vs Control (WT)
367
774
c
Volcano Plot: Combination vs Control (WT)
368
897
d
Volcano Plot: Tala vs Control (KO)
e
Volcano Plot: TAS102 vs Control (KO)
418
614
f
Volcano Plot: Combination vs Control (KO)
615
698
NS
Log2 FC
p-value
p – value and log2 FC
Log2 fold change
g
HCT116-p53WT
Tala
Combination
TAS102
h
HCT116-p53KO
i
GO Biological Process
p53WT
p53KO
DNA replication
Negative regulation of cell cycle
ECM organization
ECM structure
ECM deposition
G2/M control
DNA synthesis control
G2/M transition control
Cel cycle transition control
Positive regulation of replication
Ribosome biogenesis
ncRNA processing
Ribonucleotide complexes
rRNA metabolism
rRNA processing
tRNA metabolism
Ribosome Small subunit bio
Ribosome Large subunit bio
rRNA modification
tRNA modification
Upregulated
Downregulated
TAS
Combo
Gene count
j
HCT116-p53WT
HCT116-p53KO
Veh
Tal
TAS
TAS+Tal
Group
Condition
p53 targets
HR repair
G1/S phase
S/G2 phase
M phase
Phase
G1 phase
HR genes
M-phase
p53 Target
S/G2 genes
HCT116-p53WT
HCT116-p53KO
Vehicle
Talazoparib
TAS102
Combination
Scaled log2CPM
k
p53 Target genes
l
HR genes
m
S/G2 genes
n
M-phase genes
HCT116-p53WT
HCT116-P53KO
Z-score (Average the replicates per gene)
Veh
Tala
TAS102
TAS-Tal

Fig. 3

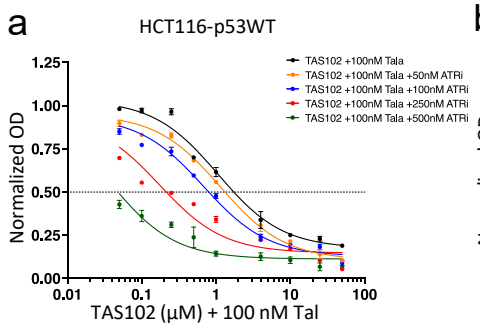

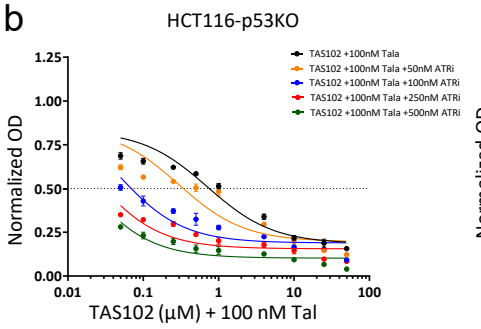

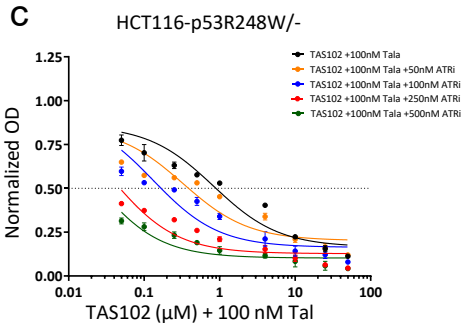

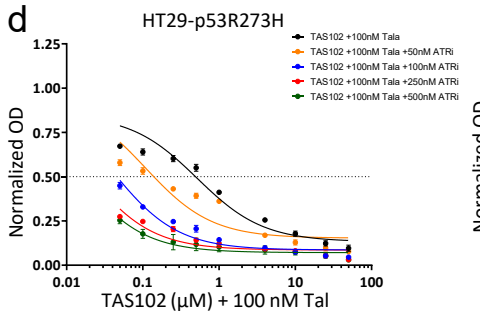

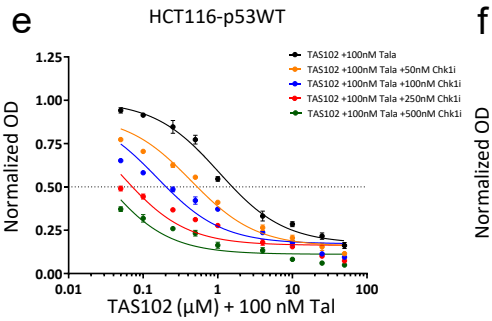

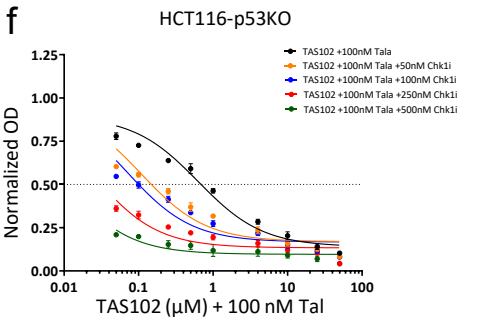

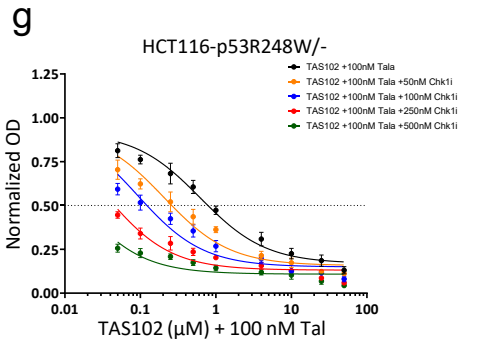

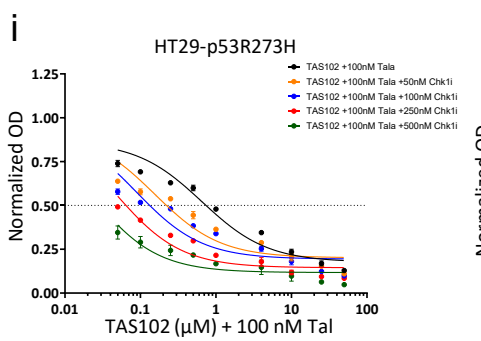

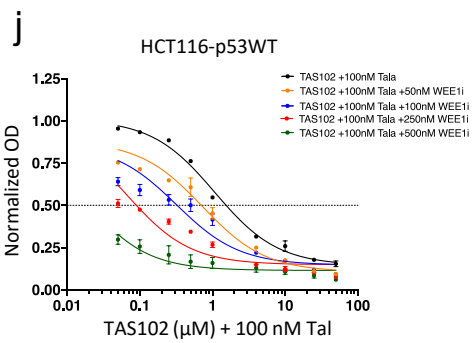

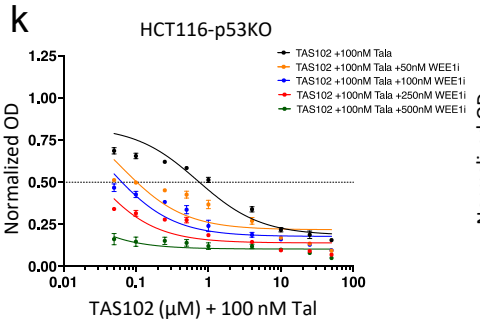

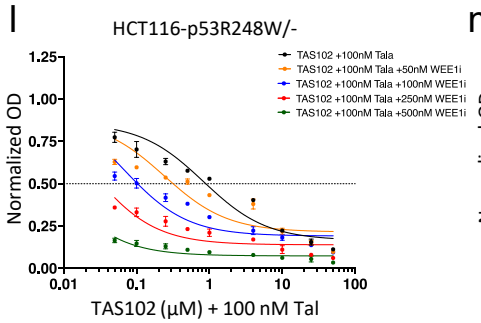

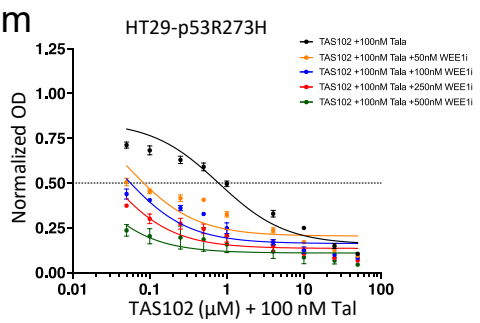

n

			ATR inhibitor		WEE1 inhibitor		CHK1 inhibitor	
Cell line	p53 Status	IC50-TAS102, μM + 100nM Tal	IC50-TAS102, μM + 100nM Tal + 100nM ATRi	Fold change at 100nM ATRi	IC50-TAS102, μM + 100nM Tal + 100nM WEE1i	Fold change at 100nM WEE1i	IC50-TAS102, μM + 100nM Tal + 100nM CHK1i	Fold change at 100nM CHK1i
MCF10A	WT	2.99 ± 0.18	2.94 ± 0.48	1.02	0.99 ± 0.49	2.90	0.13 ± 0.17	2.23
HCT116	WT	1.02 ± 0.06	0.70 ± 0.08	1.45	0.24 ± 0.15	4.64	0.15 ± 0.01	6.93
HCT116	KO	0.77 ± 0.09	0.09 ± 0.06	11.00	0.05 ± 0.01	14.09	0.11 ± 0.05	6.78
HCT116	R248W/-	0.79 ± 0.05	0.19 ± 0.08	4.16	0.10 ± 0.01	7.97	0.28 ± 0.27	3.00
HT29	R273H	0.68 ± 0.23	0.06 ± 0.04	11.33	0.08 ± 0.05	9.09	0.12 ± 0.04	5.82

o

Cell line	p53 Status	CI index ATRi	CI index WEE1i
MCF10A	WT	0.73	0.69
HCT116	WT	0.49	0.42
HCT116	KO	0.21	0.19
HCT116	R248W/-	0.24	0.30
HT29	R273H	0.30	0.16

Fig. 4

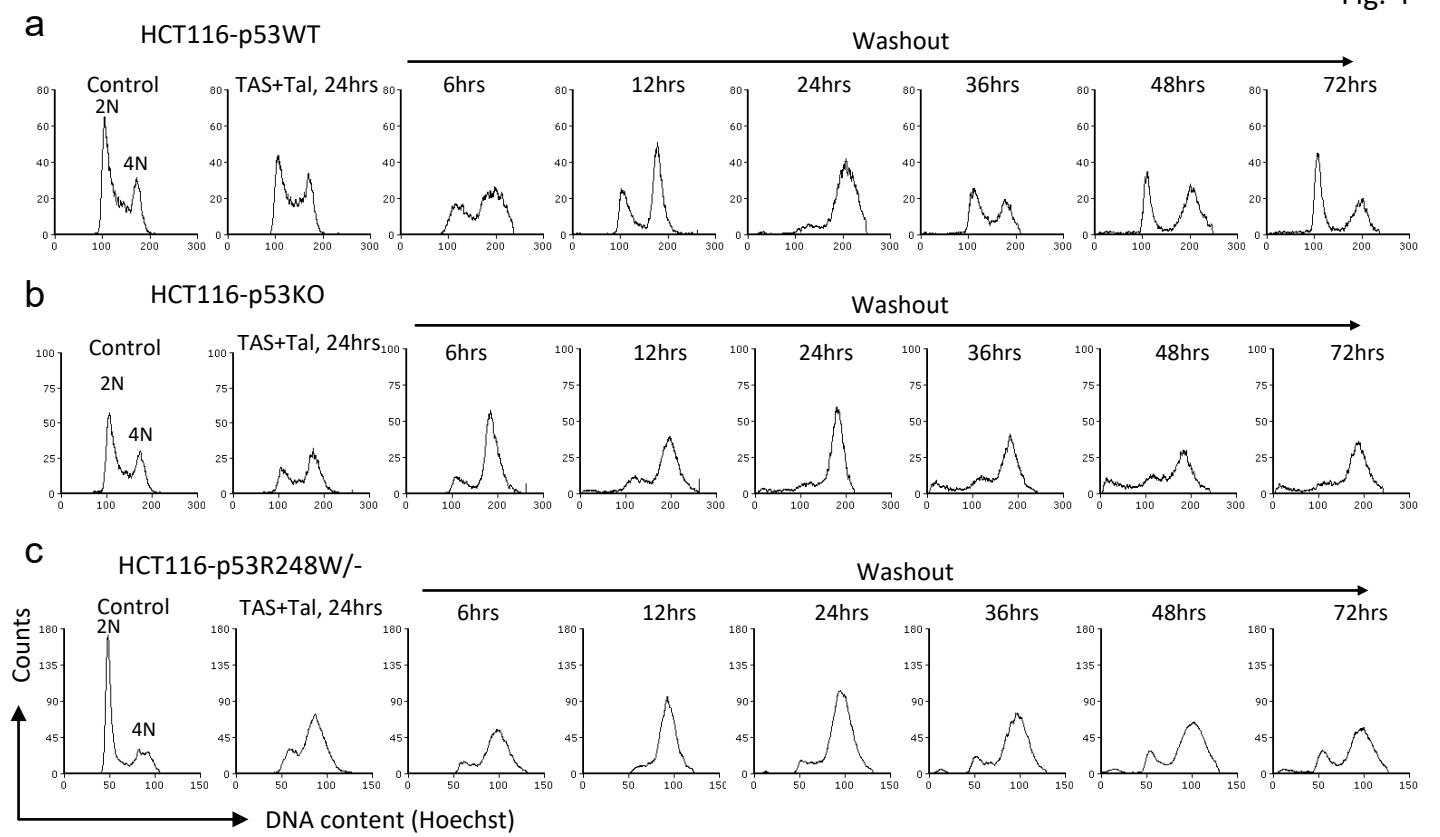
a
HCT116-p53WT
Washout
Control
TAS+Tal, 24hrs
6hrs
12hrs
24hrs
36hrs
48hrs
72hrs
2N
4N
b
HCT116-p53KO
c
HCT116-p53R248W/-
Counts
DNA content (Hoechst)

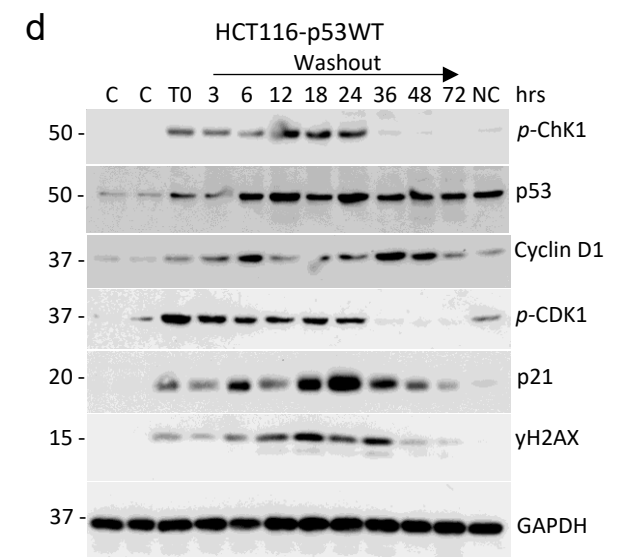
d
HCT116-p53WT
Washout
C C T0 3 6 12 18 24 36 48 72 NC hrs
p-ChK1
p53
Cyclin D1
p-CDK1
p21
γH2AX
GAPDH

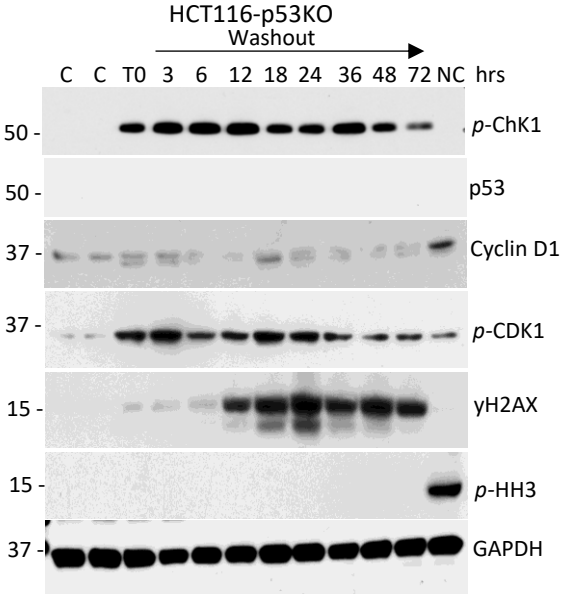
e
HCT116-p53KO
Washout
C C T0 3 6 12 18 24 36 48 72 NC hrs
p-ChK1
p53
Cyclin D1
p-CDK1
γH2AX
p-HH3
GAPDH

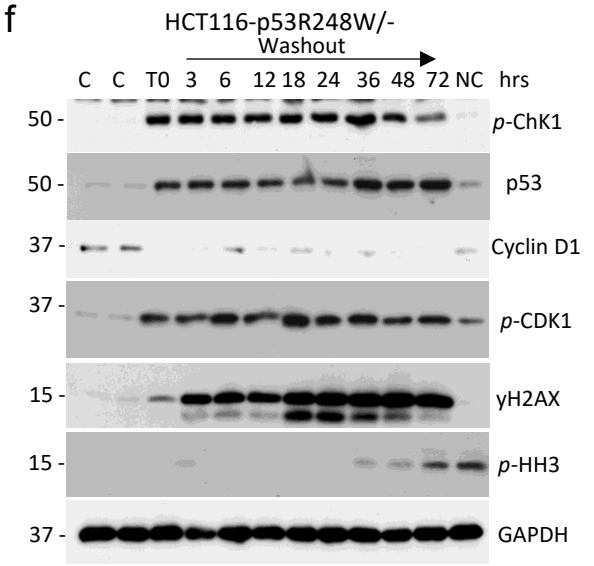
f
HCT116-p53R248W/-
Washout
C C T0 3 6 12 18 24 36 48 72 NC hrs
p-ChK1
p53
Cyclin D1
p-CDK1
γH2AX
p-HH3
GAPDH

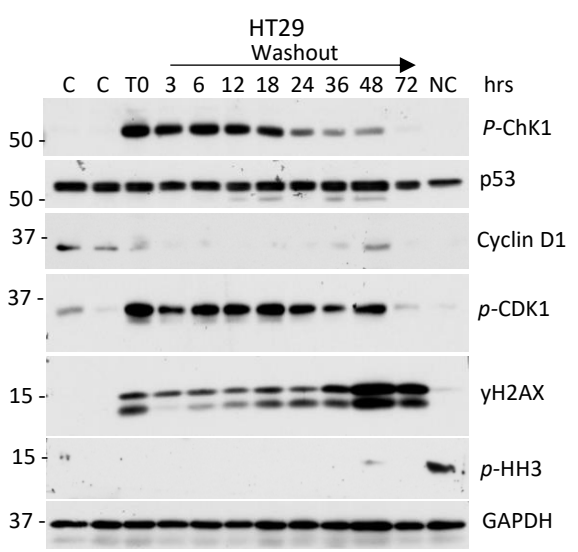
g
HT29
Washout
C C T0 3 6 12 18 24 36 48 72 NC hrs
P-ChK1
p53
Cyclin D1
p-CDK1
γH2AX
p-HH3
GAPDH

Fig. 5

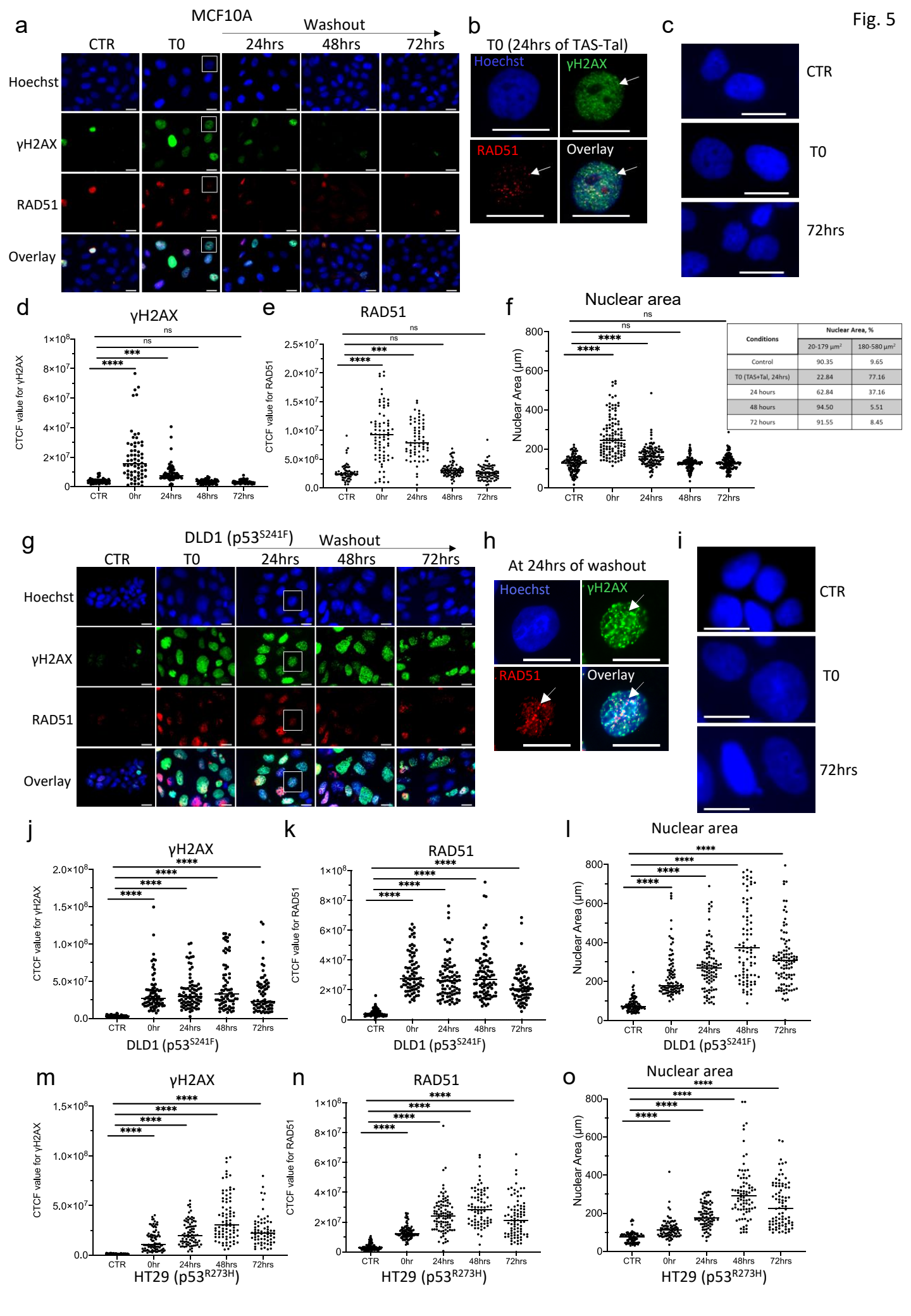

Conditions	Nuclear Area, %	
	20-179 μm²	180-580 μm²
Control	90.35	9.65
T0 (TAS+Tal, 24hrs)	22.84	77.16
24 hours	62.84	37.16
48 hours	94.50	5.51
72 hours	91.55	8.45

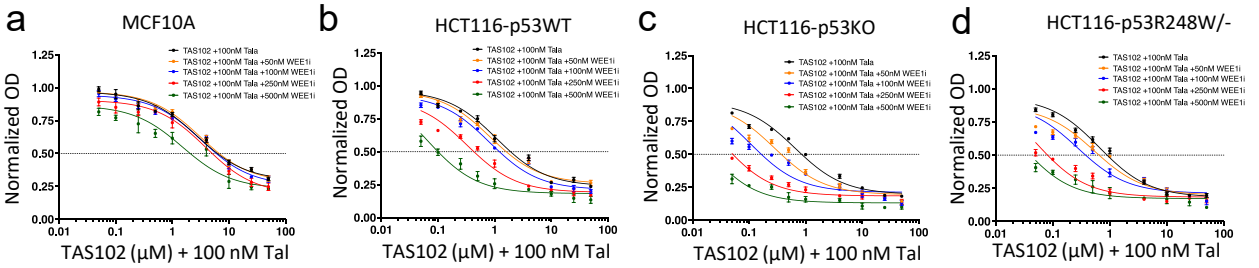

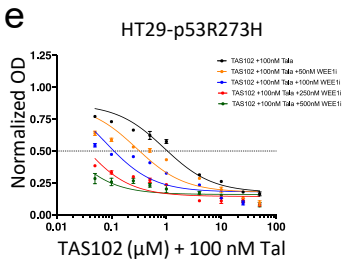

f

Cell line	p53 Status	IC50-TAS102, μM + 100nM Tal	IC50-TAS102, μM + 100nM Tal + 100nM WEE1i	Fold change at 100nM WEE1i	CI index
MCF10A	WT	3.20 ± 0.65	3.02 ± 0.36	1.07	0.94
HCT116	WT	1.19 ± 0.15	0.86 ± 0.07	1.38	0.67
HCT116	KO	0.75 ± 0.16	0.21 ± 0.15	3.57	0.31
HCT116	R248W/-	0.79 ± 0.19	0.32 ± 0.06	2.47	0.42
HT29	R273H	0.81 ± 0.16	0.12 ± 0.06	6.75	0.26

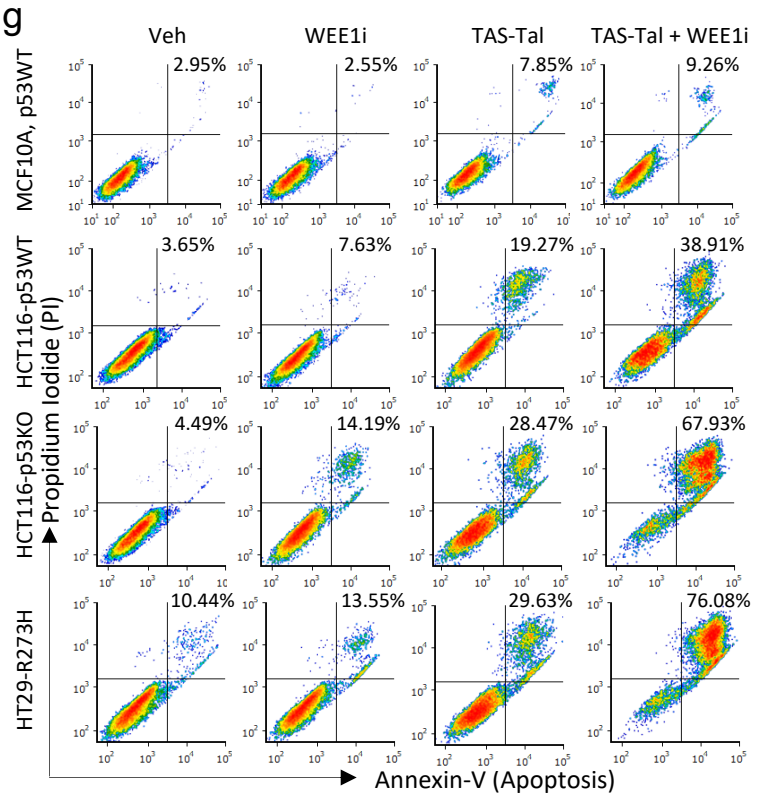

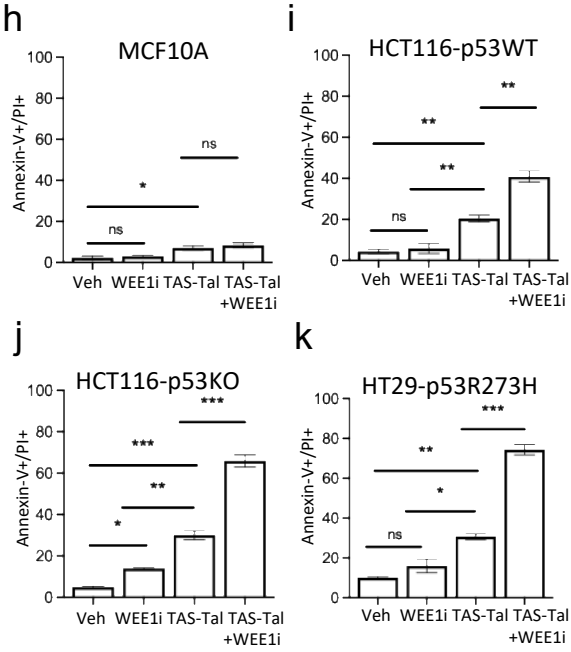

Fig. 7

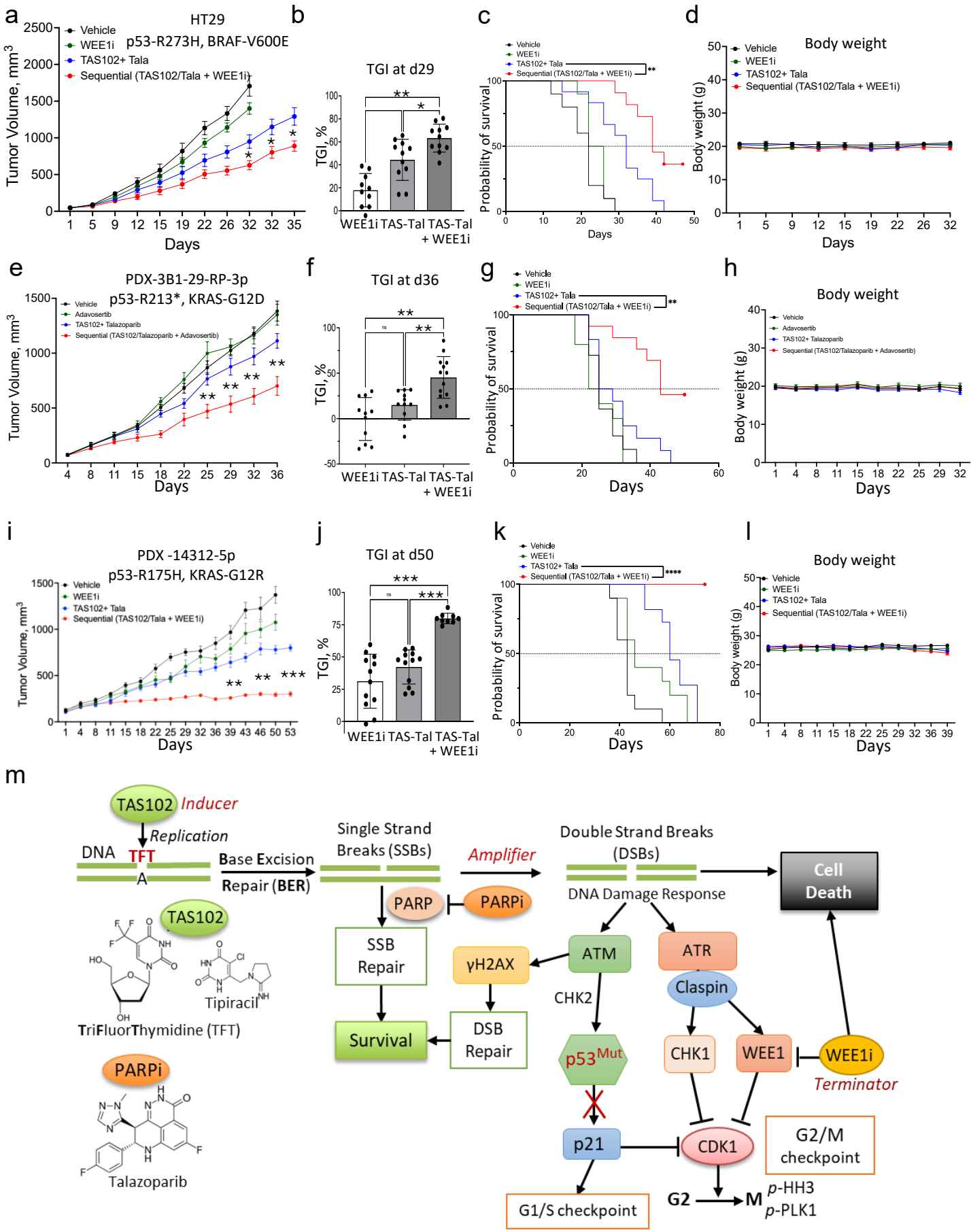
a
HT29
p53-R273H, BRAF-V600E
Vehicle
WEE1i
TAS102+ Tala
Sequential (TAS102/Tala + WEE1i)
Tumor Volume, mm3
Days
b
TGI at d29
TGI, %
WEE1i
TAS-Tal
TAS-Tal + WEE1i
c
Probability of survival
Days
d
Body weight
Body weight (g)
e
PDX-3B1-29-RP-3p
p53-R213*, KRAS-G12D
Adavosertib
TAS102+ Talazoparib
Sequential (TAS102/Talazoparib + Adavosertib)
f
TGI at d36
g
h
i
PDX -14312-5p
p53-R175H, KRAS-G12R
j
TGI at d50
k
l
m
TAS102
Inducer
Replication
DNA
TFT
A
Base Excision Repair (BER)
Single Strand Breaks (SSBs)
Amplifier
Double Strand Breaks (DSBs)
DNA Damage Response
Cell Death
PARP
PARPi
SSB Repair
γH2AX
ATM
ATR
Claspin
CHK2
Survival
DSB Repair
p53Mut
CHK1
WEE1
WEE1i
Terminator
TriFluorThymidine (TFT)
Tipiracil
Talazoparib
p21
CDK1
G2/M checkpoint
G1/S checkpoint
G2
M
p-HH3
p-PLK1